CryoSat: A mission to determine the fluctuations in Earth's land and marine ice fields ☆

D.J. Wingham [a,*], C.R. Francis [b], S. Baker [a], C. Bouzinac [b], D. Brockley [a], R. Cullen [a], P. de Chateau-Thierry [c], S.W. Laxon [a], U. Mallow [d], C. Mavrocordatos [b], L. Phalippou [c], G. Ratier [b], L. Rey [c], F. Rostan [d], P. Viau [b], D.W. Wallis [a]

[a] *Centre for Polar Observation and Modelling, University College, London, Pearson Building, Gower Street, London WC1E 6BT, United Kingdom*
[b] *ESTEC, European Space Agency, 2200 Noordwijk, The Netherlands*
[c] *Alcatel Space, 31037 Toulouse-Cedex 1, France*
[d] *EADS Astrium GmbH, 88039 Friedrichshafen, Germany*

Abstract

This paper describes the CryoSat satellite mission, due for launch in 2005, whose aim is to accurately determine the trends in Earth's continental and marine ice fields. The paper's purpose is to provide scientific users of the CryoSat data with a description of the design and operation of the SIRAL radar and the CryoSat platform, the data products, and the expected error budget. The 'low-resolution mode' (LRM), 'synthetic aperture mode' (SARM) and "synthetic aperture interferometric mode' (SARInM) of the SIRAL radar are described, together with its system parameters, its antenna gain pattern and interferometer phase difference pattern, and its calibration modes. The orbit is described, together with the platform attitude and altitude control law and control systems, and the expected pointing and altitude knowledge. The geographical masks that are used to determine acquisitions in the three SIRAL modes are described. The SIRAL data products, and the processing applied to produce them, are described. *Level 1b*, *level 2* and *higher-level* products are described in turn, with a particular emphasis on the new procedures applied to the SARInM and SARM processing over ice surfaces. The beam forming and multi-looking is summarised, and a description is given of the behaviour of the SARM and SARInM echoes over idealised surfaces. These inform descriptions of the elevation retrievals of the *level 2* processing, including the SARInM retrieval of interferometric phase. The combination of these data, through cross-over analysis over continental ice sheets, and through averaging over sea-ice, to determine areal averages of ice sheet elevation change or sea-ice thickness, is described. The error budget in these higher-level products is described, together with its breakdown into errors arising from the instrument and errors arising from the retrievals. The importance of the co-variance of these errors in determining the final error is stressed. The description of the errors also includes a summary of the experiments required following the launch to validate the CryoSat mission data. An estimate of the mission performance over ice surfaces is made at various spatial scales, and it is concluded that even the relatively short, three-year duration of the CryoSat mission will allow it to make an important scientific contribution, particularly when combined with results from earlier satellite missions.
© 2005 COSPAR. Published by Elsevier Ltd. All rights reserved.

Keywords: CryoSat satellite mission; Earth's continental and marine ice fields; SIRAL radar; CryoSat platform

1. Introduction

Fluctuations in the mass of the Earth's marine and grounded ice sheets have profound implications for the Earth's radiation balance, ocean circulation and

sea-level that, in the 21st century, may have considerable political and economic consequences (IPCC, 2001). Global, coupled, climate models predict that warming will substantially destroy the multi-year Arctic sea-ice, accelerating regional climate change. Reductions in sea-ice and increasing run-off from the Greenland ice sheet will alter the wind and buoyancy forcing of the Arctic Ocean and the Greenland–Iceland–Norwegian (GIN) and Labrador Seas. This may affect the North Atlantic overturning circulation as a whole and with it the climate of north-west Europe (e.g., Broecker, 1987; Rahmstorf et al., 1996). Warming of Antarctic circumpolar and shelf seas at depth may, through interaction with the Antarctic ice shelves (Jacobs et al., 1992), affect Southern Ocean deep-water formation and ventilation. Ice shelf melting, glacial–interglacial sea-level rise, and internal dynamics may combine to alter even the stability of the grounded West Antarctic ice sheet, a reservoir of 5 m of eustatic sea-level (Oppenheimer, 1998). A warming atmosphere is alone sufficient to shrink the Greenland ice sheet. Even were radiative forcing to stabilise within the next 50 years, the Greenland ice sheet will contribute some 10 cm/century to sea-level for centuries to come. Finally, while the world's $\sim 10^5$ small glaciers and ice caps constitute only 5% of the total land-ice reservoir, their location exposes them to changes in climate. Their reduction in mass may be the largest ice contribution to 21st century sea-level rise (Meier, 1984).

Within the past few years, new, detailed illumination of the changes in land and marine ice is transforming our understanding of the mass budgets and their changes (Fig. 1). This information is provided by satellites carrying active microwave radars to high latitudes, and in particular the decade long time series provided by the ERS satellites' altimeter and synthetic aperture radar (SAR). The altimeter measurements have accurately constrained to -60 ± 76 Gt yr^{-1} the mass balance of 63% of the Antarctic ice sheet (Wingham et al., 1998). Moreover, a combination of SAR interferometry and satellite altimetry (Rignot, 1998; Shepherd et al., 2002 and Fig. 1(a)) have shown that dynamically-related thinning is penetrating deep into the interior of the West Antarctic, Pine Island and Thwaites drainage basins-the region long thought most susceptible to on-going retreat through externally-driven changes. Even more recently Laxon et al. (2003) have used ERS altimetry to provide the first synoptic measurements of Arctic sea-ice thickness (Fig. 1(b)). These observations show that Arctic sea-ice is far more variable than believed hitherto, fluctuating interannually in volume by 10%, and that ice thermodynamics, rather than dynamics, determine the total annual balance.

These discoveries are the more remarkable for having used, opportunistically, a 1970s pulse-limited altimeter design intended originally to measure the marine geoid (McGoogan, 1975). In consequence, the spatial

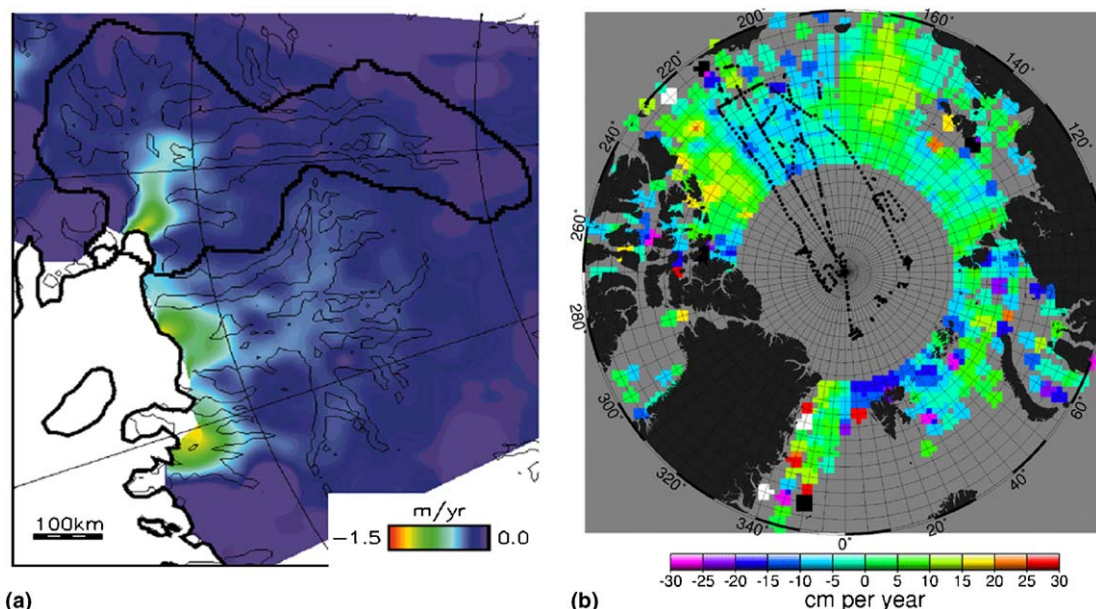(a)   (b)

Fig. 1. (a) The first direct measurements of grounded Antarctic ice sheet mass loss to the ocean, revealed by ERS measurements of the Pine Island and Thwaites Glaciers' drainage basins, in the West Antarctic ice sheet (WAIS). The correlation of the thinning with the surface velocity contours (fine lines), determined with ERS SAR-interferometry, is evidence that the source of the thinning is ice dynamics. (Redrawn from Shepherd et al., 2001 and 2002.). (b): The first synoptic measurements of Arctic sea ice thickness, from the ERS-1 and ERS-2 radar altimeters, provide the trend in multi-year ice thickness 1993–1999. Dotted lines indicate the location of upward-looking sonar (ULS) measurements 1993–1997. The perceived mid-1990s Arctic-wide decrease of 10 cm year^{-1} (Rothrock et al., 1999) deduced from the sparse submarine measurements, is clearly related to the inadequate spatial coverage.

resolution of ∼10 km, and on-board echo accumulation system, limits their application to observations of ice fluxes. Sea ice thickness measurements are restricted to the largest 5% of floes and thus only 5% of the measurements are useful, limiting the detailed study of the forcing of the ice by the atmosphere and ocean. The spatial resolution also restricts investigation of ice sheet flow to the largest ice streams of Antarctica; the measurements have too poor a quality to illuminate the behaviour of much of the Antarctic Peninsula, many of the Greenland flows, and the small ice caps and glaciers around the world. In addition to these limitations of the payload is the 98.5° inclination of the ERS (and ENVISAT) satellites. Studying the flux of sea-ice to its main export conduit through the Fram Strait, and completing the picture of West Antarctic Ice Sheet fluctuations by including the Ross Ice Shelf streams A and B, requires observations beyond the latitudinal limit of 81.5°.

These limitations have led to the development for ice observations of optical, laser altimeters, of which the first was launched in 2002 on the 94° inclination, US satellite ICESAT (Zwally et al., 2002). On the other hand, the all-weather capability of the pulse-limited radar, and the relative in-expense of using mature technology, has led in Europe to the selection of a beam-forming radar altimeter, 'SIRAL', as the main payload of the European Space Agency (ESA) 92° inclination, 'CryoSat' satellite, whose purpose is to provide continuous synoptic measurements of Earth's land and marine ice fluxes. To the authors' knowledge, the first use of beam-forming altimetry for planetary mapping was the Russian Venera-15 and -16 missions to Venus (Alexsandrov et al., 1998), but the SIRAL design in fact owes more to Earth-specific concept studies of the 1990s which were guided by the heritage of existing, pulse limited hardware (Jensen and Kilgus, 1993; Raney, 1995; Raney, 1998; Phallipou et al., 1998; Jensen, 1999). SIRAL employs the along-track beam formation to generate a resolution cell of approximately ∼300 m × 1 km (as compared with ∼10 km of the pulse-limited systems and ∼70 m of the laser systems).

CryoSat is due for launch in 2005, and is the first in-orbit flight of an altimeter of its kind. The purpose of this paper is to provide, in a single location, an end-to-end description of the mission. Any such description is necessarily selective. In making selections we have aimed to provide the information needed by scientific users of the CryoSat data. In Section 2, we describe the design and operation of the SIRAL, the CryoSat platform, in so far as its sensors and control system affect the orbit and attitude of the radar, and the ground control of the SIRAL data acquisitions. Section 3 provides a description of the *level 1* data processing and products – essentially, along-track ordered radar echoes. Because this processing, and the resulting echoes, differ from that of previous, pulse-limited altimeters, we also give a description of the behaviour of the radar echoes over simple surfaces. In Section 4, we describe the *level 2* data processing and products – essentially, along-track ellipsoidal elevations. Here we have emphasised the processing of the data over land- and sea-ice, which are new procedures, and summarise only briefly the processing of the pulse-limited mode data in view of its similarity to previous missions such as ERS, ENVISAT and TO-PEX/Poseidon. The same approach is taken in Section 5, which describes the *higher-level* processing needed to generate spatially and temporally averaged ice fluxes of the kind illustrated in Fig. 1. These sections all inform Section 6, which describes the error budget of the products, and outlines approaches to their post-launch validation. In conclusion, Section 7, we comment briefly on the projected performance in the light of the mission goals. Two appendices provide details of the function used in the retracking, and of the angle error budget.

In writing this paper, we have drawn freely from earlier documents, notably the original mission proposal and its later reincarnation, the CryoSat Mission Requirements Document (Wingham, 1999), the CryoSat Mission and Data Description (Francis, 2001), and the CryoSat Calibration and Validation Concept Document (Wingham et al., 2001). In addition we have made use of the results of pre-launch performance tests on the engineering or flight model hardware. On the other hand, the paper also contains new material. The description of the *level 1b* and *level 2* processing and their resulting errors has not been given before (Sections 3, 4 and some of 6), the impulse response of a 'line' beam Eq. (14) is new, and the result Eq. (19), a correction of the pulse-limited echoes for the ellipticity of the antenna pattern, is also new. In general, we believe that bringing the information together in a single paper is worth the cost of some repetition.

2. The CryoSat satellite

In this section, the design and operation of the CryoSat satellite (Fig. 2) measurement and control systems is given, together with the in-orbit operation of the payload. The SIRAL is described in Section 2.1, the orbit and attitude characteristics in Section 2.2, and the operations in Section 2.3.

2.1. The SIRAL instrument and measurements

The SIRAL instrument is a 13.6 GHz, normal incidence radar altimeter mounted at the front of the satellite (Fig. 2). It consists of the antenna subsystem, radiofrequency unit (RFU) and digital processing unit (DPU). The antenna subsystem comprises two nadir looking, Cassegrain antennas mounted perpendicular to the flight direction on an 'optical' bench, constructed
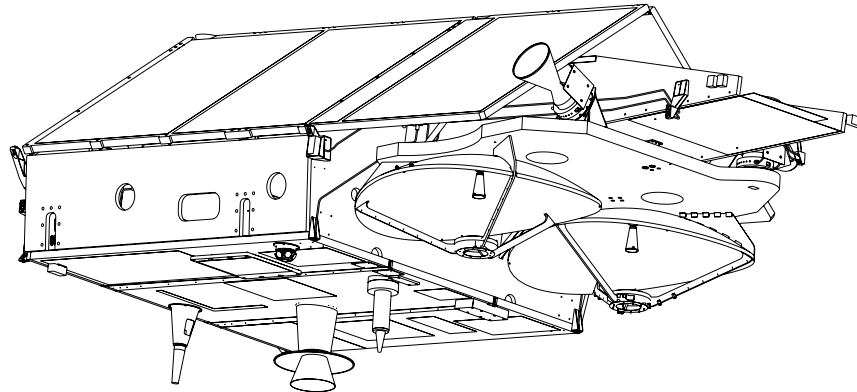
Fig. 2. The CryoSat satellite configuration. The two SIRAL antennas and optical bench are mounted near the front of the spacecraft (in the direction of motion) in the across-track direction. Three star trackers are mounted on the zenith face of the bench. The SIRAL electronics are mounted directly above the antennas; the protruding panel at the very front is a thermal radiator. The platform systems are mounted on the internal nadir panel, which also supports the DORIS antenna, radar retroreflector, and S-band and X-band command and telemetry antennas. The Earth facing nadir panel is the 'cold' panel used to radiate unwanted heat. The body-mounted, Ga-As solar panels are over-sized to accommodate the non-sun-synchronous orbit.

of carbon-fibre reinforced plastic. The bench in turn is mounted on the spacecraft structure using isostatic mounts. The antennas' waveguides, made of invar, are connected via a duplexer to the RFU and thence the DPU, which are mounted on the sky-facing side of the front spacecraft structure. The design minimises the effect of thermal distortion when the antennas are used as an interferometer. The bench and waveguide materials provide a very low thermal expansion coefficient, and the RFU location minimises the waveguide

length. Heat from the DPU and RFU is dissipated by the radiator that forms the very front of the spacecraft. In flight, the entire system is wrapped in multi-layer insulation, while thin sheets of germanium-coated kapton cover the antennas' reflectors to reduce the effect of asymmetric solar heating.

SIRAL employs 'full deramp' pulse compression (MacArthur, 1976). A summary of the SIRAL instrument characteristics is given in Table 1. The DPU and RFU together have a single transmission chain, con-

Table 1
SIRAL instrument characteristics

	Measurement mode		
	LRM	SARM	SARInM
Receiver chain[a]	Left[a]	Left[a]	Left and Right[a]
Carrier frequency (GHz)		13.575	
Antenna gain (dB)		42	
Along-track antenna 3 dB width		1.0766° (full beamwidth)	
Across-track antenna 3 dB width		1.2016° (full beamwidth)	
Transmitted (measured) bandwidth (MHz)		350 (320)	
Transmitted power (W)		25	
Transmitted (measured) pulse duration μs		49 (44.8)	
Pulse repetition interval	1971 Hz	18.182 kHz	18.182 kHz
Burst repetition interval (ms)	–	11.7	46.7
Samples per echo	128	128	512
Measurement range window (m)	60	60	240
Measurement range gate (m)		0.46875	
Interferometer baseline (m)	–	–	1.172
Tracking samples per echo		128	
Tracking range window (m)	60	60	480
Tracking range gate (m)	0.469	0.469	3.75
Number of tracking echoes averaged per 46.7 ms update cycle	91	32	24
Data rate	51 kbps	12 Mbps	24 Mbps
Power consumption (W)	95	130	125
Mass (kg)		61	

[a] To an observer astride the satellite, facing in the flight direction, with his feet in the direction of Earth.

nected via the duplexer to the antenna to the left of the flight direction. The 49 μs chirp is digitally generated in the DPU, allowing two bandwidths, 350 and 40 MHz, to be transmitted via a 25 W, solid-state amplifier in the RFU. The RFU and DPU also have two receive chains, one for each antenna.

The use of the antennas on reception, the timing of the transmitted chirps, and the transmitted bandwidth, depend on the operating 'mode'. There are three operating modes, 'low resolution' mode (LRM), 'synthetic aperture' mode (SARM), and 'synthetic aperture interferometric' mode (SARInM). LRM provides for conventional, pulse-limited altimetry using a single antenna. SARM provides for along-track aperture synthesis using a single antenna. SARInM allows for along-track aperture synthesis using two antennas, and for phase comparison (interferometry) between the echoes received on each antenna. The SARM and SARInM are collectively referred to as high-bit-rate (HBR) modes.

In LRM, the instrument operates with a pulse-repetition frequency (PRF) of 1.971 kHz (Fig. 3). Every 507, a 49 μs, 350 MHz bandwidth chirp is transmitted. Some 4.8 ms later, the echo from Earth is received on the same antenna, passed through the duplexer to the RFU, deramped, amplified, anti-alias filtered and returned to the DPU for analogue-to-digital (A/D) conversion. In LRM, 128, 8-bit, I and Q samples are formed at a sampling rate of 0.35 μs (only 44.8 μs of the echo is

recorded, which reduces the measurement bandwidth to 320 MHz.) A complex spectrum sampled at 22.3 kHz is formed from these samples via a fast-Fourier transform (FFT) and this spectrum is power detected. Ninety-one consecutive echoes are accumulated (to reduce speckle noise), and passed to the logic (the 'tracker') that provides closed-loop control of the timing of the deramp chirp and the receiver gain. These same, averaged, 'spectral domain' echo powers also form the measurement (i.e. the telemetered) data of the LRM mode. With these parameters, the LRM measurement and tracking spectrum spans a 'range window' of 60 m with a range resolution (sampling interval) of 0.46875 m.

The LRM measurements are those of a conventional, pulse-limited altimeter, save that (for reasons of launcher accommodation) the antennas are slightly narrowed in the along-track direction, resulting in a slightly asymmetric antenna pattern (Fig. 4(a)). Within 3 dB of the boresight, this pattern is accurately described by the function

$$G(\theta, \vartheta) = G_0 \exp\left[-\theta^2 \left(\frac{\cos^2\vartheta}{\gamma_1^2} + \frac{\sin^2\vartheta}{\gamma_2^2}\right)\right], \tag{1}$$

where θ and ϑ are, respectively, the polar and azimuthal directions measured with respect to the antenna boresight, and with $\gamma_1 = 0.0133$ and $\gamma_2 = 0.0148$. G_0, the peak gain, equals 42 dB. Eq. (1) describes a pattern in which gain lines fall on ellipses. At the nominal altitude (Section 2.3) the LRM signal-to-noise ratio (SNR) is
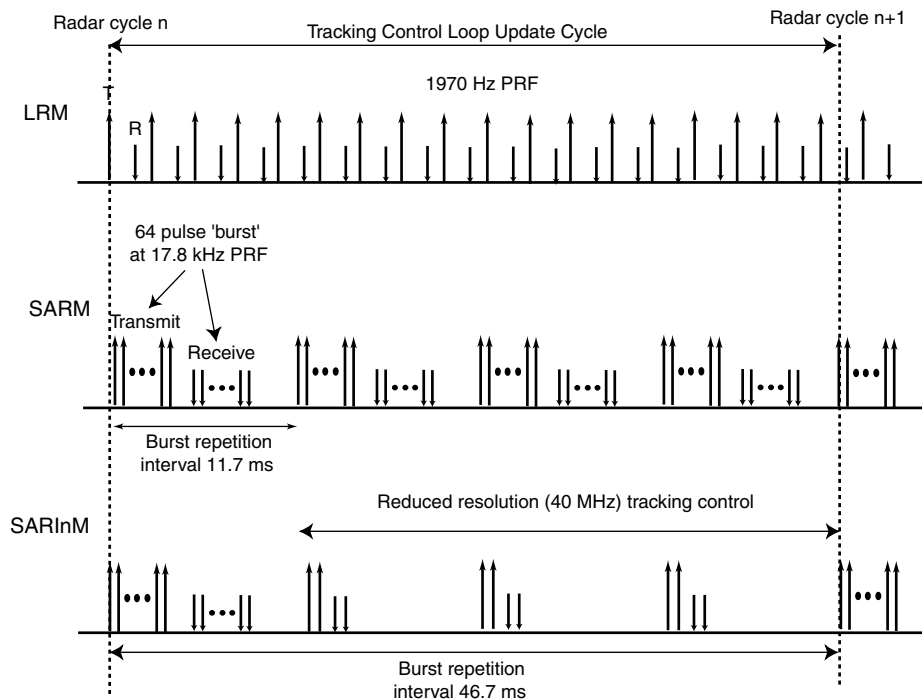

Fig. 3. SIRAL transmission and reception timing in the three measurement modes. LRM, low resolution mode; SARM, synthetic aperture mode and SARInM, synthetic aperture, interferometric mode. Together with the changes in transmission timing are changes in the sampling of the received echo. See text for details.
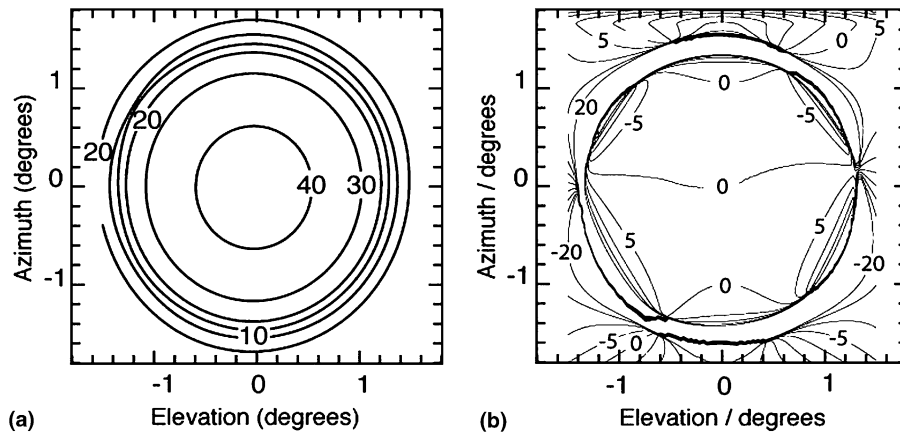
Fig. 4. (a): The Cryosat antennas' one-way gain pattern. Contours are in dB. In the satellite coordinate frame, 'elevation' refers to the along-track direction. (b): The interferometer phase difference pattern. Contours are in degrees of phase difference.

8 dB when the system is operated over a uniform spherical surface, of an Earth radius, and backscattering coefficient of −10 dB. The antennas are linearly polarized with an orientation parallel to the interferometer baseline.

In SARM, the same receive chain is used, but the mode differs in the timing of its transmissions and the formation of the measurement data (Fig. 3). The pulses are transmitted in groups, 'bursts', of 64 pulses with a PRF of 18.182 kHz. During a burst, the carrier phase is locked to the transmission timing so that the transmissions within the burst are phase coherent. Each burst is transmitted with a burst-repetition frequency (BRF) of 87.5 Hz. The length of the burst, 3.6 ms, and the interval between the bursts, 11.7 ms, are sufficient for the echoes from a transmitted burst to be sent via the duplexer to the receive chain before the next burst is transmitted (a 'closed' burst arrangement).

During the reception of a burst, the timing of the deramp chirp is held constant (to avoid introducing differential phase shifts between the transmissions of the burst). As in LRM mode, echoes are power detected and accumulated (over 46.7 ms) to provide closed loop control. However, in contrast to the LRM, the measurement data comprise the 128, I and Q, 'time-domain' samples of each individual echo, directly from the A/D converters. As with the LRM, the SARM tracking spectrum spans a range window of 60 m with a range resolution of 0.469 m, as will the measurement spectrum, once the data are processed on ground.

In SARInM, a 350 MHz, 64 pulse, 18.182 kHz PRF burst is again transmitted, but with a lower BRF of 21.4 Hz (Fig. 3). The echoes are directed via the duplexer to the two receive chains. The timing of the deramp chirp is identical for each chain (so as not to introduce differential phases between the two receive chains). In contrast to SARM, the sampling interval at the A/D converters is reduced to 0.0875 μs and 512, 8-bit, I and Q samples are generated for each receive channel. The

SARInM measurement data comprise these time-domain samples of each individual echo from each receive channel, directly from the A/D converters. The decrease of sampling interval means that the SARInM spectrum spans a range window of 240 m with a range resolution of 0.469 m, once the data are processed on ground.

However, in contrast to the LRM and SARM, the SARInM measurement data are not used to inform the closed-loop control of the instrument. Instead, the longer interval (of 46.7 ms) between the measurement bursts is employed to transmit 40 MHz bandwidth pulses. The echoes from these pulses are received on a single channel, sampled at 0.35 μs, passed through the FFT, power detected and accumulated over the 46.7 ms interval. The resulting averaged, spectral-domain power provides for the closed-loop control of the instrument. This spectrum spans a range window of 480 m with a resolution of 3.75 m. This arrangement provides the SARInM with a tracking range window larger than that of the measurement range window (480 m versus 240 m) to provide for robust closed-loop control over regions on Earth of significant topography.

In addition to the operational modes, SIRAL has an acquisition mode (ACQM) that is used to initialise the closed loop control, and two calibration modes, 'CAL1M' and 'CAL2M'. The CAL1M calibrates the DPU and RFU signal paths (excluding the transmission amplifier and duplexer) for the deramp chirp timing and the receiver gain, intra-burst phase rotations (which provide phase calibration to the aperture synthesis) and the SARInM phase difference as functions of frequency and automatic gain control (AGC) setting. A 64-pulse burst is directed through an attenuating connection between the transmission and receive chains to achieve this. The deramp chirp frequency is offset to allow the calibration to be made at 11 frequencies lying within the measurement spectrum. CAL2M provides detailed corrections for the variation of receiver gain across the measurement spectrum. It is implemented by averaging

repeated measurements of the noise power in the absence of a transmission. Finally, a second calibration path is included to provide at a single frequency a SAR-InM phase difference calibration that includes the duplexer. This calibration (known for historical reasons as 'CAL4') is not a separate mode, but is performed with a repetition frequency of 1 Hz from within the SAR-InM. It provides a correction for phase difference as a function of time; the total phase difference correction (a function of frequency, AGC setting and time) is obtained by combining this value with that of the CAL1M.

The SIRAL instrument control is updated following a cycle of activities – the 'radar cycle' – at intervals of 46.7 ms (equal to the burst repetition interval in SAR-InM). The measurement data is blocked in so-called 'source packets', and there is a fixed number of source packets per radar cycle. In LRM there is one packet per radar cycle, in SARM and SARInM four packets per cycle. Any particular packet is related to the first of the cycle by a counter. The datation of the measurement data is provided by the start of the radar cycle. The DORIS receiver (Section 2.2) generates an accurate *Temps Atomique International* (TAI) time at 1 Hz. Associated with this time is a pulse, which is used to trigger an 80 MHz counter within the SIRAL. At the start of the radar cycle, this counter is read, and its value is placed into the data measured during that cycle. This effectively stamps the data with the time at which the radar cycle commences. In SARM and SARInM the time of any particular transmission can then be found by determining its position within its burst, and the position of this burst with respect to the first of the radar cycle. In LRM, the situation is slightly more complicated. During radar cycle (see Fig. 3), 91 echoes are measured. During radar cycle $n + 1$ these echoes are FFT'd, power detected and averaged (see above). This process is completed within the interval of the radar cycle, and the average of the echoes measured during cycle are written in the source packet containing the time at which cycle $n + 1$ commences.

2.2. CryoSat orbit and attitude characteristics

CryoSat will be launched from Plesetsk, Russia, on a Rokot Launcher (which is based on an SS19 missile) into near circular, near polar orbit with an average altitude of 717.2 km and an eccentricity of 0.0014. The orbit inclination is 92°, which is a compromise between the desire to achieve a high density of orbit cross-overs at high latitudes (for land ice altimetry), while having more-or-less complete coverage of the Arctic Ocean and the Antarctic continent. The repeat period is 369 days (5344 revolutions, average velocity 7389 m s^{-1}, 7.5 km inter-track spacing at the Equator) which provides the high orbit cross-over density (10 crossovers km^{-2} year^{-1} at 87°). The orbit also has a 30-day subcy-
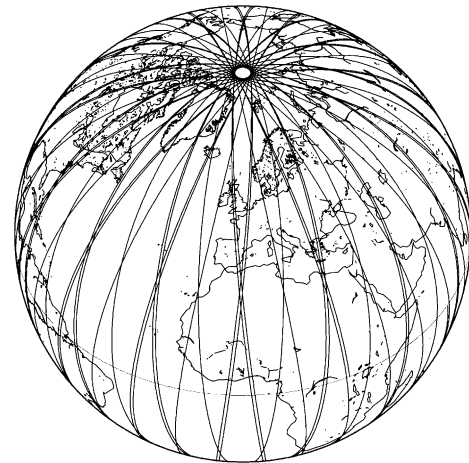

Fig. 5. The 92° inclination CryoSat orbit. The illustration shows the orbits accumulated over a period of three days. This is sufficient to illustrate the coverage of the Arctic Ocean, and to indicate the rapid increase in orbit cross-over density that occurs as the latitude approaches 88°.

cle, which provides every 30 days uniform coverage of the Arctic sea-ice (see Fig. 5). (The term 'subcycle' means that the full, 369-day repeat is built up by successive shifts of the 30-day repeat pattern.)

Knowledge of the orbit is provided by the DORIS receiver located centrally in the nadir panel of the spacecraft (Fig. 2). The DORIS system (Tavernier et al., 2003) comprises a network of more than 50, globally distributed beacons. Each beacon transmits two stable frequencies (2036.25 and 401.25 MHz) that are received every 10 s by the DORIS receiver when the beacon is in sight. Using an on-board ultra-stable oscillator, the Doppler shift of these signals is determined and yields, essentially, the line of sight velocity between the beacon and the satellite. The use of two frequencies allows the ionospheric total electron content to be estimated and the satellite velocity compensated for the variation of electromagnetic wavespeed through the ionosphere. The set of radial velocities received from all the beacons provide a dense set of tracking data for the computation of the orbit.

The messages uplinked from the beacons include time signals that allow the DORIS receiver time reference to be synched to TAI, which provides at 1 Hz the time reference for CryoSat as a whole and the SIRAL (Section 2.1) in particular. The DORIS receiver also includes software for the real-time computation of the orbit, the DORIS 'navigator' orbit, which provides the CryoSat platform with its position. This orbit, which is estimated to be accurate to 30 cm in the radial direction, is also included into the measurement data, so that good quality orbital parameters are available on the ground prior to the precise orbit determination (POD) from the DORIS observations.

The payload also includes a laser retro-reflector (LRR), mounted (see Fig. 2) at the front left of the nadir panel. The LRR consists of seven corner-cubes, a nadir looking cube surrounded by six off-nadir cubes in a hexagonal arrangement. As a whole, the LRR provides for measurements at any satellite elevation greater than 20° from the horizon, for all azimuths. The LRR is included to provide verification of the orbit accuracy independently of the DORIS system. It provides an estimated radial accuracy of 0.6 cm.

The orbit is maintained within a dead band of ±1 km at the Equator. (When the satellite is higher than the nominal altitude its velocity is slower than the nominal velocity, and the tracks drift eastwards. As the satellite does work against atmospheric drag, the altitude falls, and once it crosses the nominal altitude, the tracks drift westward. When the orbit coincides with the nominal track, the orbit is raised, and the sequence starts again.) Four, 40 mN cold-gas thrusters maintain the orbit. The propellant is gaseous nitrogen, stored in a 132 l tank initially at 276 bar, located in the heart of the satellite at its centre of gravity.

The attitude of the platform and SIRAL in particular is provided by three star trackers. The trackers are mounted on the zenith side of the SIRAL optical bench to provide as accurately as possible the interferometer attitude. The star tracker consists of a camera head, which images a $22° × 22°$ field of view onto a $1024 × 1024$ charge-coupled device (CCD) array. The pattern of stars recorded on the CCD array is compared with an onboard catalogue, and the attitude in an inertial reference frame is output from the tracker at 1.7 Hz. The star tracker heads are contained within baffles to avoid sun or moon blinding (it is the baffles that are visible in Fig. 2). Pre-launch tests provide an estimated measurement accuracy in satellite roll of 27″ ($1.1 × 10^{-4}$ rad). The attitude data are dated in an essentially similar fashion to the SIRAL data. The values of a 50 MHz clock in the star-tracker at the time of the DORIS 1 Hz pulse and at the mid-interval of the star tracker integration time are attached to the data. These two values are used to datate the data.

Two other attitude sensors are mounted on the platform: a coarse Earth–Sun sensor, and two, three-axis magnetometers, which provide attitude and attitude-rate with respect to the geomagnetic field. These provide the attitude for the 'rate damping mode', 'coarse pointing mode' and 'safe mode'. The attitudes provided by the star trackers, and the position provided by the DORIS navigator orbit, are used to control the spacecraft attitude in 'fine-pointing mode'. The spacecraft control law is defined in terms of a local coordinate system defined as follows. Let $\hat{\mathbf{n}}_v$ be the direction of the satellite velocity viewed from Earth, and let $\hat{\mathbf{n}}_n$ be the direction, from the satellite, of the local normal to the WGS-84 ellipsoid. $\hat{\mathbf{n}}_v$ and $\hat{\mathbf{n}}_n$ define a plane (the 'along-track' plane). Let $\hat{\mathbf{n}}_2$

lie in this plane and be orthogonal to $\hat{\mathbf{n}}_n$. (If the orbit is parallel to the ellipsoid, $\hat{\mathbf{n}}_2 = \hat{\mathbf{n}}_v$, but this is generally only approximately the case.) Let $\hat{\mathbf{n}}_3 = \hat{\mathbf{n}}_n × \hat{\mathbf{n}}_2$. The control law is then to maintain the SIRAL antennas' boresights in the direction $\hat{\mathbf{n}}_n$, and the interferometer baseline parallel to $\hat{\mathbf{n}}_3$ (i.e. the satellite is yaw steered). The system is designed is to obey this law to within 0.2° about any axis. (The reference attitude of the 6° forward tilt of the antennas relative to the spacecraft, visible in Fig. 2, is to minimise gravity-gradient torques.) The control is provided by three magnetotorquers, which provide torques about axes orthogonal to the direction of the magnetic field, and by sixteen, 10 mN attitude control thrusters, fed by the cold gas system. (The cold gas system is also responsible for initial acquisition of the orbit following launch, and for other orbit manoeuvres such as collision avoidance. Because CryoSat is limited to a cold gas system, the usage of the fuel is an important factor in the total mission lifetime.)

2.3. SIRAL operations

The default SIRAL operating modes are determined using a geographic mask. An example of a mask is shown in Fig. 6. This mask divides the Earth's surface into zones, which are designated LRM, SARM, SAR-InM or no measurement. Two weeks prior to the event, a predicted orbit is run over the mask and the time of mode switches determined. These switches are uplinked to the satellite in the week prior to their operation. The mask is not fixed, but may be updated at two weekly intervals, and in particular the mask will be updated at monthly intervals to allow for the variation of the extent of sea-ice during the year. In addition to the mask-driven operation, time-tagged SIRAL modes may be commanded directly. Examples of these are SIRAL calibration modes, or mode use designed to support ground experiments whose purpose is external calibration of the SIRAL modes or validation of the SIRAL data. The location accuracy of a mode switch on a satellite track is 30 km. On the other hand, SIRAL is designed to maintain echo tracking control during a switch between measurement modes, and the break in data continuity between switches of measurement modes is 700 m.

The Cryosat data are accumulated in a 256 Gbit onboard memory and downlinked to ground when the satellite is in sight of its ground station, located at Kiruna, Sweden. Passes of the satellite in sight of Kiruna occur on average for 10 of 14 orbit revolutions per day, with four successive 'blind orbits'. This design provides coverage in the HBR modes of the ice surfaces whose behaviour is the primary mission goal (see Fig. 6). More extensive use of the SARM and SARIM is limited by data volume and power constraints. Nonetheless, there is some system margin for wider use of these modes,
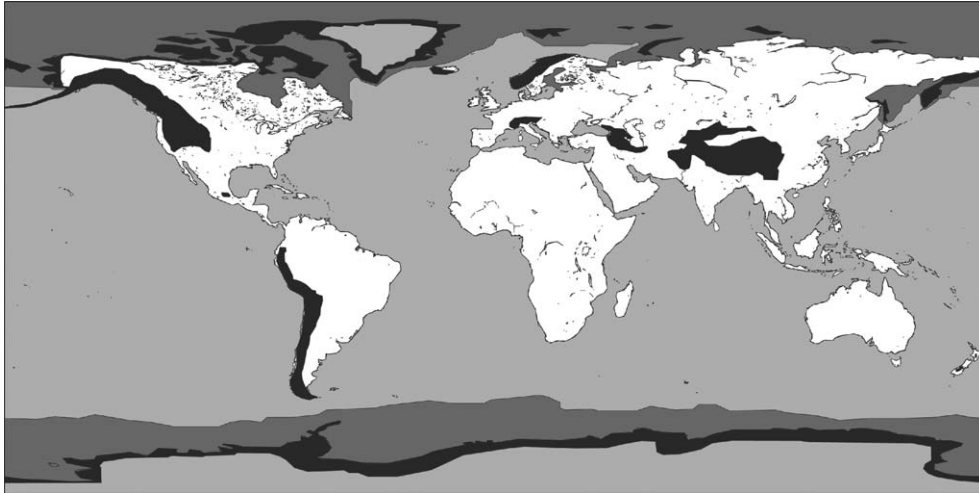
Fig. 6. A SIRAL mode acquisition mask. Over the ice sheet margins and temperate land ice, SARInM (black) will be used. Over the sea ice, SARM (dark grey) will be used. Over the Antarctic and Greenland interiors, and the ocean, LRM (light grey) will be used. This mask is an illustration; the actual mask will be complicated by, e.g. HBR acquisitions over the ocean for calibration.

and there will be some coverage of the ice-free ocean in SARM and SARInM.

3. CryoSat *level 1b* data processing and products

CryoSat data telemetered to ground by the satellite are termed *level 0* data. These data are passed through serial processors to generate products that are distributed to users. The *level 1b* processor generates, essentially, an average echo for each location along the ground track; the *level 2* processor generates, again essentially, an elevation for each location along the satellite track; *higher-level* products (which are not supplied by the ESA ground segment) generate gridded maps of, for example, sea-ice thickness or trends in ice sheet elevation. This section describes the first of these steps, the *level 1b* processing and data.

The data flows associated with the *levels 1* and *1b* processing of the data are shown in Fig. 7. The processing proceeds in two stages. In the first stage, the internal calibration data are applied, and the data are geolocated and oriented using the output of the DORIS system and the star trackers. The calculation of the precise orbit from the DORIS *level 0* data is itself a complex procedure that is not described here (see e.g., Nouel et al., 1994).

3.1. High-bit-rate (HBR) mode range compression and beam formation

The *level 1b* processing of the SARM and SARInM, the HBR modes, have a great deal in common. In the HBR modes, a sequence of processing steps is performed on the data, outlined in Fig. 7. First, the *level*
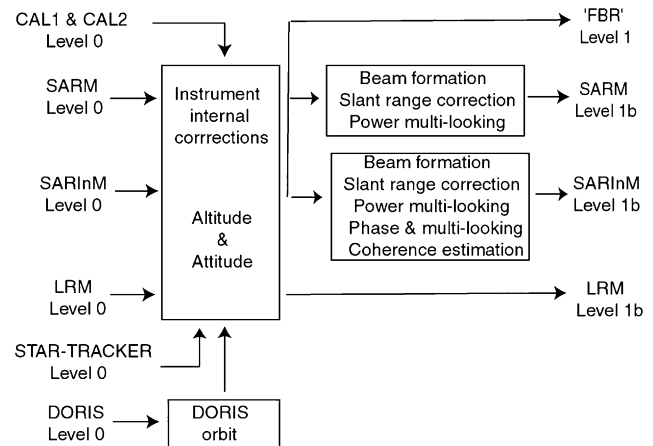

Fig. 7. Overview of CryoSat *level 1b* processing.

0 data is re-blocked into bursts, instrument corrections are performed, and the bursts are geo-located.

The geo-location of the data makes use of the 'start–stop' assumption. The round-trip time of an echo is some 4.8 ms, and in this interval the satellite travels some 33 m. In this interval, the motions of the satellite and the echo map out approximately a triangle whose vertex is the scattering point on the ground. It may be shown that, because the satellite speed is very much smaller than the electromagnetic wave speed, the received echo is indistinguishable from the echo that would have been observed had the satellite been stationary at a known point on the orbit approximately half way between those of transmission and reception. In geo-locating the bursts, each individual echo is treated as if it were so measured. In the HBR modes, each burst has 64 individual echoes, with 64 corresponding 'start-stop' locations. This burst location, which is denoted

$\mathbf{x}_b$ below, is then the mid-point of these locations, lying half way between the 32nd and 33rd individual 'start–stop' locations.

The instrument-corrected, geo-located bursts form a *level 1* product termed the 'full bit-rate' (FBR) data. The FBR data also form the input to the next stage of the HBR processing, the range compression. At this stage, each FBR burst is a discrete complex function of elapsed time, and position, centered about $\mathbf{x}_b$, along the orbit. The range compression is completed by FFT-ing the data over elapsed time, forming a function of position and frequency, or, equivalently, of echo delay time t. (In LRM, the range FFT is completed on-board.)

Over the interval of the burst, the satellite moves some 61 m along its orbit. This is short enough it may be considered a straight line in the direction $\hat{\mathbf{n}}_v$. Further, because of the shortness of this length in comparison with the altitude and because the antenna restricts the surface illumination to a narrow range of angles about the nadir direction, the echoes ϕ received from an elemental scatterer on the surface are distinguished within a burst only by the change in carrier phase. This depends on the position within the burst, and on the interferometer baseline. One may then write for the mth echo φ of the burst following the temporal FFT

$$\varphi^{(\pm)}(\mathbf{x}_b, t, m) = \sum_k \phi_k(\mathbf{x}_b, t) e^{\pm i k_0 B \hat{\mathbf{n}}_k \cdot \hat{\mathbf{m}}_b/2}$$
$$\times \exp[2i(m - 65/2)\Delta k_0 \hat{\mathbf{n}}_k \cdot \hat{\mathbf{n}}_v] \quad m \in [1, 64].$$
(2)

Here, Δ is the along-track sampling interval, k_0 the carrier wave-number, and $\hat{\mathbf{n}}_k$ the direction of the kth elemental scatterer. $\hat{\mathbf{m}}_b$ is the direction vector of the interferometer baseline, and B its length. The notation $\varphi^{(\pm)}$ distinguishes the right- and left-hand antennas; it will be used only when the distinction is needed. The summation is over all elemental scatterers. The power of the echo is $\varphi\bar{\varphi}$, where the overbar denotes conjugate, and the 'mean' power is the expectation $\langle\varphi\bar{\varphi}\rangle$ over the ensemble of elemental scatterers.

These echoes are input to the next stage of the processing, the 'beam formation'. The echoes are phase weighted and summed over position to provide new echoes ψ given by

$$\psi^{(\pm)}(\mathbf{x}_b, t, \theta_l) = \frac{1}{8} \sum_{m=1}^{64} \varphi^{(\pm)}(\mathbf{x}_b, t, m) \exp[-2ik_0\Delta\theta_l(m - 65/2)].$$
(3)

That this results in beam formation may be seen by substituting for φ in Eq. (3) with Eq. (2) to obtain

$$\psi^{(\pm)}(\mathbf{x}_b, t, \theta_l) = \sum_k \phi_k(\mathbf{x}_b, t) e^{\pm ik_0 B\hat{\mathbf{n}}_k \cdot \hat{\mathbf{m}}_b/2} d(\hat{\mathbf{n}}_k \cdot \hat{\mathbf{n}}_v - \theta_l),$$
(4)

where

$$d(x) = \frac{\sin[64\Delta k_0 x]}{8\sin[\Delta k_0 x]}.$$
(5)

The normalisation by 1/8 is explained in Section 3.5.

The echoes ϕ are those arising when the surface is illuminated by the antenna, whose one-way, power gain pattern is shown in Fig. 4. Eq. (4) shows that the echoes ψ are those arising from an illumination that is the product of the (one way, power) antenna pattern with the 'beam' pattern d. This is a function of direction only. It takes a constant value on directions that form a cone centered at $\mathbf{x}_b$ and with an axis of revolution containing $\hat{\mathbf{n}}_v$. In any plane containing $\hat{\mathbf{n}}_v$, it is only a function of the cosine of the angle defining the cone, or, equivalently, the sine of its complement, which we write as $\sin\vartheta$. The maximum of the beam is defined by the cone $\sin\vartheta = \theta_l$. θ_l is termed the 'look angle' of the beam. The behaviour of d in the along-track plane in the vicinity of $\sin\vartheta = \theta_l$ is shown in Fig. 8(a). More generally, there are many such beams, because the denominator in Eq. (5) has zeroes whenever $\sin\vartheta - \theta_l$ is an integer multiple of $\pi/\Delta k_0$. At the average velocity, the separation between the repeated maxima is 1.52°. However, as already noted, the echo ψ arises from an effective illumination that is the product of the beam gain and the antenna gain. Fig. 8(b) compares the spacing of the repeated beams with the antenna pattern in the along-track plane. It may be seen that the repeated beams fall outside the antenna main lobe and are strongly attenuated.
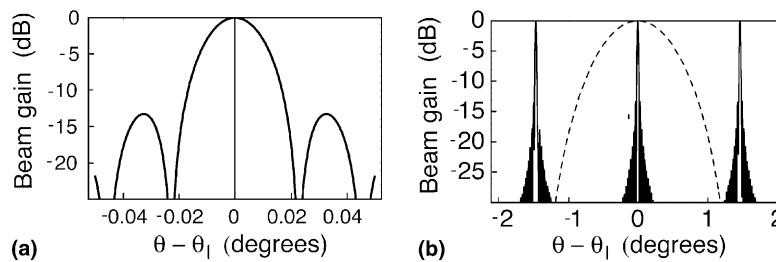

Fig. 8. (a): The main lobe and first side lobes of the beam gain pattern at the nominal platform velocity. The 3 dB width is 0.022°. (b) The beam gain (solid line) compared with (dashed line) the antenna gain in the along track plane. For the beam formed parallel to the antenna boresight, the 'ambiguous' beams fall outside the antenna main lobe, and are strongly attenuated by the antenna gain pattern.

While we refer to the use of Eq. (3) as 'beam formation', it would be termed 'unfocussed aperture synthesis' in the context of synthetic aperture theory (see e.g., Curlander and McDonough, 1991) – hence the terms 'SAR' and 'SARIn' modes. It is also possible by a change of variable to replace the look angle with a Doppler frequency describe a beam as a 'Doppler' beam. We use angle as the transform variable because of its direct relation with the viewing geometry.

The narrowness of the antenna pattern in the along and across track directions allows other simplifications. The antennas' boresights are held almost normal to the velocity vector (see Section 2.2). In consequence, the cone $\sin \vartheta = \theta_l$ passing through the antennas' pattern has a very small curvature, so small that the beam maximum may be regarded as lying in the tangent plane to the cone that contains $\hat{\mathbf{n}}_3$. They also allows the approximation $\sin \vartheta \sim \vartheta$ in the argument of the beam pattern, as has been done in Fig. 8.

In principle, a beam may be formed at any look angle using Eq. (3). In practice, the processor restricts the look angles to the set $\theta_l = \theta_r + \pi n/(64 k_0 \Delta)$, $n \in [-31, 32]$. This allows Eq. (3) to be implemented as a phase weighting, followed by a 64-point FFT. This restriction results in 64, beams with an equal angular separation, such that the maximum of the $(n+1)$th beam falls at the first zero of the nth. At the average velocity, this separation is 0.0238° (see Fig. 8(a)). The angle θ_r is termed the 'rock' angle of the beam. Its purpose is described shortly.

In practice, the power $\psi \bar{\psi}$ from any one beam fluctuates due to 'speckle', the exponentially-distributed fluctuation arising from the random phase of the elemental scatterers. This fluctuation is reduced by 'multi-looking' the echo (Section 3.5). This process sums the echoes from beams directed at the *same* location from *successive* bursts to form an average whose fluctuations are reduced. This require that beams from successive bursts are directed at the same location on the surface. However, the surface is a priori unknown. Thus an estimate of the surface, the 'assumed' surface, is used to direct the beams.

The assumed surface is determined by interpolating along track the range given by the on-board echo gating control (Section 2.1). For the first burst processed, the rock angle θ_r is adjusted so that the $n = 0$ beam is directed at the nadir point of the burst (i.e., removes the small lack of orthogonality between $\hat{\mathbf{n}}_v$ and $\hat{\mathbf{n}}_n$). This results in 32 forward-looking beams and 31 backward-looking beams equally spaced in angle by 0.0238°. The intersection of these angles with the assumed surface determines a sequence of points. The normal projections of these points onto the ellipsoid, i.e., onto the track, are spaced by approximately 297 m. On the other hand, the next burst occurs 77 m along-track in SARM and 309 m in SARInM. If θ_r were held constant, the beams formed from this next burst will not coincide on the assumed
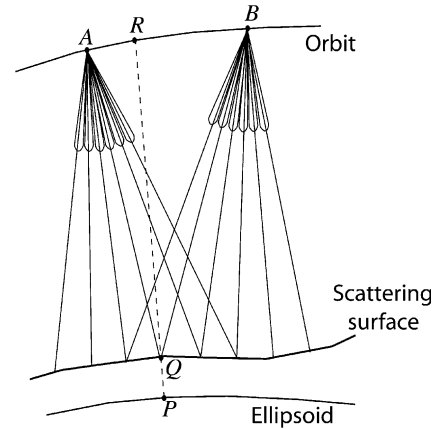

Fig. 9. The geometry of the multi-looking and slant range correction. A burst located at *A* on the orbit illuminates a set of 64 locations on the surface, approximately 294 m apart and lying approximately within ±0.76° of the nadir point at *P*. The beam rock angle directs the central beam at the nadir point *P*, which defines a set of points on the assumed surface. A little while later, a burst located at *B* also illuminates 64 locations. The beams of burst *B* are 'rocked' by up to a beam width to bring those of its beams that overlap beams from other bursts into exact coincidence on the points on the assumed surface. *Q* is such a point. Those points from the burst at *B* that do not overlap existing points define new points on the assumed surface at which beams from future bursts are directed. For clarity, only a few beams are shown, and the angles are grossly exaggerated.

surface with those of the previous burst, so θ_r is adjusted, burst to burst, to bring the beam maxima from separate bursts into coincidence at the samples on the assumed surface. The range of θ_r is limited to be less than a beam separation angle (0.0238°), so that, sooner or later, the 32nd forward looking beam will be directed at a previously undefined point on the assumed surface. This point is taken to define a new point, and the process continues. It is illustrated in Fig. 9.

3.2. Power and phase behaviour of the echoes

At *level 2*, the elevation and other properties of the surface is determined from the echo power and phase resulting from the *level 1b* processing. In detail, these are rather complicated functions of delay-time. To understand them, we describe first their behaviour for a beam thin enough it may be regarded as a line, and with the compressed pulse regarded as infinitely narrow. This allows the behaviour to be understood entirely from geometric considerations. We then describe the detailed effects of the finite width of the beams and the finite compressed pulse duration.

For this purpose, we introduce a local, Cartesian coordinate system with its origin at the point $\mathbf{x}_s$ of the stack (the point *Q* in Fig. 9 is an example). The *z*-axis is parallel to $\hat{\mathbf{n}}_n$, with the *x*-axis lying in the along track plane, and the *y*-axis across track. Because the beam is very thin, a point on the surface illuminated by the beam

lies in the plane of the beam maximum, and therefore has coordinates $\{0, y_s, z_s\}$. Any beam directed at the point will have arisen from a burst location $\mathbf{x}_b$ whose coordinates are[1] $\{x_b, 0, z_b\}$. The echo from any point on the surface will occur at a delay

$$
\begin{aligned}
t_z &= \frac{2}{c}(x_b^2 + y^2 + (z_0 + (z_b - z_0) - z_s(y_s))^2)^{1/2} \\
&\sim \frac{1}{c}\left(z_0 + z_b + \frac{x_b^2}{z_0} + \frac{y_s^2}{z_0} - 2z_s(y_s)\right).
\end{aligned} \tag{6}
$$

Here, z_0 is the z-coordinate of the orbit at $x = y = 0$. (For example, with the origin of the local system at the point Q in Fig. 9, z_0 is the z-coordinate of the point R.) With this approximation (the Fresnel approximation) the delay separates into four known terms (the first four on the right of Eq. (6)) and one unknown term, associated with the location of the surface.

Two of the known terms, the second two on the right-hand side of Eq. (6), depend on the location of the burst. This dependence is removed in the processor by advancing the delay of each echo so as to make them functions of

$$
t_{sr} = t - \frac{1}{c}\left(z_b - z_0 + \frac{x_b^2}{z_0}\right) \tag{7}
$$

a procedure termed 'slant range correction'. With the slant range correction, the echo from the surface occurs at a delay time t_{zsr}, namely

$$
t_{zsr} = \frac{2}{c}\left(z_0 + \frac{y_s^2}{2z_0} - z_s(y_s)\right). \tag{8}
$$

With reference to Fig. 9, the correction removes the difference in delay between the path AQ (or BQ) and RQ. In the limit of a 'line' beam and narrow compressed pulse, the remaining range delay then has no dependence on look angle. (Slant-range correction is termed 'delay compensation' by Raney (1998) and 'range migration' in synthetic aperture radar theory (Curlander and McDonough.)

We now turn to the dependence of the echo on the across-track geometry. This depends generally on the shape of the surface. However, in order to design the *level 2* elevation retrieval (Section 4), some model of the surface must be assumed. The model we use here is that of a uniformly rough surface, inclined at some angle to a sphere with an Earth radius. This model, while not accounting for all the topographic variation of the surface, has proved in the past a suitable starting point for the design of the elevation retrieval algorithm.

Since we wish to account for Earth curvature, we introduce a circle of Earth radius R lying in the across-track plane and passing through the point $\mathbf{x}_s$

(so that the y_s-axis forms a tangent to the circle). A point on the circle is identified by the angle ϕ subtended between it and the point $\mathbf{x}_s$, and, in this coordinate system, the elevation $z_e(\phi)$ of any point on the scattering surface is the distance to it measured normally from the circle. Then $y_s = (R + z_e)\sin\phi$ and $z_s = (R + z_e)\cos\phi - R$, and to the same order of approximation as already used

$$
t_{zsr} = \frac{2}{c}\left(z_0 + \frac{2R^2\eta}{z_0}\sin^2\phi/2 - z_e(\phi)\right). \tag{9}
$$

Here $\eta = 1 + z_0/R$ is a geometric factor that describes the departure of the sphere from a plane.

We now consider the phase difference between the echoes at the two antennas. In general, this is a function of the cosine of the angle between the interferometer baseline and the arrival direction of an elemental scatterer, or equivalently the sine of its complement ρ. If the attitude control works perfectly, the baseline lies in the across-track plane. With the assumptions we have made, one may write

$$
k_0 B \sin\rho \sim k_0 B \frac{R}{z_0}\sin\phi \tag{10}
$$

for this phase difference. Similarly, the antenna gain Eq. (1) is approximately separable into its along and across track components, and may be written

$$
G \sim G_0 \exp(-(\theta_1/\gamma_1)^2)\exp(-(R\sin\phi/(z_0\gamma_2))^2).
$$

Consider now a surface that is inclined across-track at angle β to the circle of the local coordinate system, i.e. $z_e = R\sin\phi\tan\beta$, with a uniform backscattering coefficient σ^0. In the 'line' case we are considering, one may show that the mean value of the cross-product of the echoes at the two antennas is

$$
\begin{aligned}
&\langle \psi^{(+)}\bar{\psi}^{(-)}(t_{sr}, \theta_1)\rangle \\
&\sim \frac{\lambda^2 D_0 \sigma^0 G_0^2 R}{4\pi^3 z_0^3}\exp\left(-\frac{2\theta_1^2}{\gamma_1^2}\right) \\
&\times \int_{-\pi}^{\pi}\mathrm{d}\phi \quad \times \exp\left(-\frac{2R^2\sin^2\phi}{z_0^2\gamma_2^2} + ik_0 B\frac{R}{z_0}\sin\phi\right) \\
&\times \delta\left(t_{sr} - \frac{2}{c}\left(z_0 + \frac{2R^2\eta}{z_0}\sin^2\phi/2 - R\tan\beta\sin\phi\right)\right),
\end{aligned} \tag{11}
$$

where

$$
D_0 = \int_{-\infty}^{\infty}\mathrm{d}u\,\mathrm{d}^2(u). \tag{12}
$$

It is convenient to define a new time origin by putting $\tau = t_{sr} - 2z_0/c$. Integration of Eq. (11) provides

$$
\langle \psi^{(+)}\bar{\psi}^{(-)}(\tau, \theta_1)\rangle \sim 0 \quad c\eta\tau < -z_0\tan^2\beta, \tag{13}
$$

---

[1] This ignores the slight out-of-plane curvature of the orbit. For most surfaces, the effect of this is negligible.

while for $c\eta\tau > -z_0\tan^2\beta$,

$$\langle\psi^{(+)}\bar{\psi}^{(-)}(\tau,\theta_1)\rangle$$

$$\sim \frac{\lambda^2 D_0 \sigma^0 G_0^2 c}{8\pi^3 z_0^{5/2}} \exp\left(-\frac{2\theta_1^2}{\gamma_1^2}\right)\frac{1}{(c\eta\tau+z_0\tan^2\beta)^{1/2}}$$

$$\times e^{-\frac{2}{\gamma_2^2}\left(\frac{c\tau}{\eta z_0}+\frac{2}{\eta^2}\tan^2\beta\right)+i\frac{k_0 B}{\eta}\tan\beta}\left[e^{-\left(\frac{4}{\gamma_2^2\eta^2}\tan\beta-ik_0 B\right)\left(\frac{c\tau}{z_0\eta}+\frac{1}{\eta^2}\tan^2\beta\right)^{1/2}}\right.$$

$$\left.+e^{\left(\frac{4}{\gamma_2^2\eta^2}\tan\beta-ik_0 B\right)\left(\frac{c\tau}{z_0\eta}+\frac{1}{\eta^2}\tan^2\beta\right)^{1/2}}\right]. \qquad (14)$$

Setting $B = 0$ in this expression provides the mean power $\langle\psi\bar{\psi}(\tau,\theta_1)\rangle$.

Eqs. (13) and (14) offer considerable insight into the behaviour of the echoes. First, the earliest arrival occurs when $c\eta\tau = -z_0\tan^2\beta$. (This is correct to $O(\beta^4)$, the difference arising from the Fresnel approximation.) For delay time greater than this, the echo power varies $z_0^{-5/2}$ (as observed by Raney, 1998) reflecting that the instrument is beam-limited along-track, and pulse-limited across-track. In practise, the dominant variation of echo power with delay arises from the term $(c\eta\tau + z_0\tan^2\beta)^{-1/2}$; the contribution of the antenna is slowly varying in comparison. This term decays rapidly with delay time, in contrast to a purely pulse-limited system, whose decay is determined by the more slowly varying antenna gain. (As is illustrated later, the integrable singularity when $c\eta\tau = -z_0\tan^2\beta$ is removed once a finite pulse duration is considered.)

Turning to the phase, the leading term is $k_0 B/\eta)\sin\beta$ which is correct to $O(\beta^3)$. This phase corresponds to the direction of the earliest arrival. More generally there are two contributions in Eq. (14) to the power and cross-product. The geometric reason for this is illustrated in Fig. 10. For 'smooth' surfaces, a constant range intersects the across-track surface in two locations. The phase of the two contributions nearly, but not exactly, cancel, because, as Fig. 10 illustrates, the antenna gain they experience differs. This imbalance between the two terms causes the total phase to depart from $k_0 B/\eta)\sin\beta$ as the delay-time increases. An expansion of Eq. (14) provides

$$\text{Arg}\left[\langle\psi^{(+)}\bar{\psi}^{(-)}(\tau,\theta_1)\rangle\right] \sim \frac{1}{\eta}k_0 B\tan\beta$$

$$\times\left(1-\frac{4}{\gamma_2^2\eta^3 z_0}(c\tau\eta+z_0\tan^2\beta)\right)$$

$$\times c\eta\tau+z_0\tan^2\beta > 0, \qquad (15)$$

which shows that this departure is linear in delay time τ (as noted first by Jensen, 1999). With $\tan\beta$ positive, the slope is negative, because greater weight is given by the antenna gain to the arrival closer to its axis, causing the observed phase to take a smaller value.
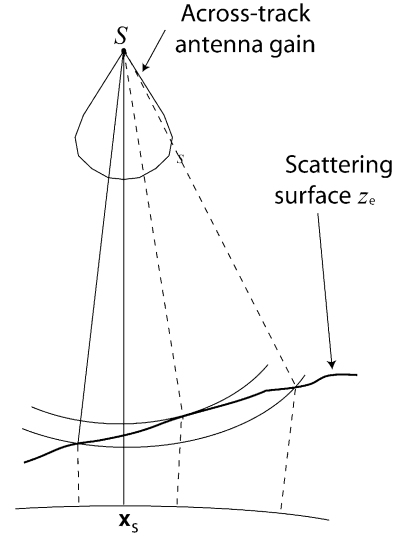

Fig. 10. The across-track geometry of the interferometer in the coordinate system used in the text. In the across-track plane, the surface defines a line whose elevation is its normal separation from a circle of approximately an Earth radius. The earliest arrival of the echo at the satellite at S is from the point of closest approach (POCA). For 'smooth' surfaces, this point is unique. For this arrival time, the interferometer phase uniquely determines the across track location of the POCA. At later delays, a line of constant delay intersects the surface at, generally, many locations. The total phase of the echo then depends on the difference in the phase of the various contributions and the difference in antenna gain they each experience. For simple surfaces like the one shown, and that discussed in the text, there are generally two such contributions. Angles are shown grossly exaggerated for clarity.

This description is altered to an extent by the effects of finite pulse duration and beam width. Fig. 11(a) shows the iso-delay lines to a surface inclined to spherical Earth that fall within 2 km of the point of closest approach (POCA). (If the surface has no inclination with respect to the sphere, the POCA coincidences with the nadir point.) The lines are separated in delay by resolution of 3.125 ns. Superimposed on these are the locations (shown dashed) of the maxima of the beams; at the average velocity and altitude their separation Δ_b is 297 m. Three beams (that is, three look angles) are singled out. Fig. 11(b) shows the mean echo power and mean echo phase as functions of delay-time for these three look angles. In these plots, the echoes are slant range corrected, and the origin is the time of earliest arrival. Taking the power first, the $\tau^{-1/2}$ decay of Eq. (14) is apparent in all three. However, in the vicinity of the earliest delay origin, the singular behaviour of Eq. (14) has been smoothed.

The resulting power shows an important distinction from a conventional, pulse-limited system: the point on the echo corresponding to the surface does not lie at the half-power point of the leading edge, but rather closer to the maximum.

The power also shows an important distinction from Eq. (14), in that the shape of the echo has a strong
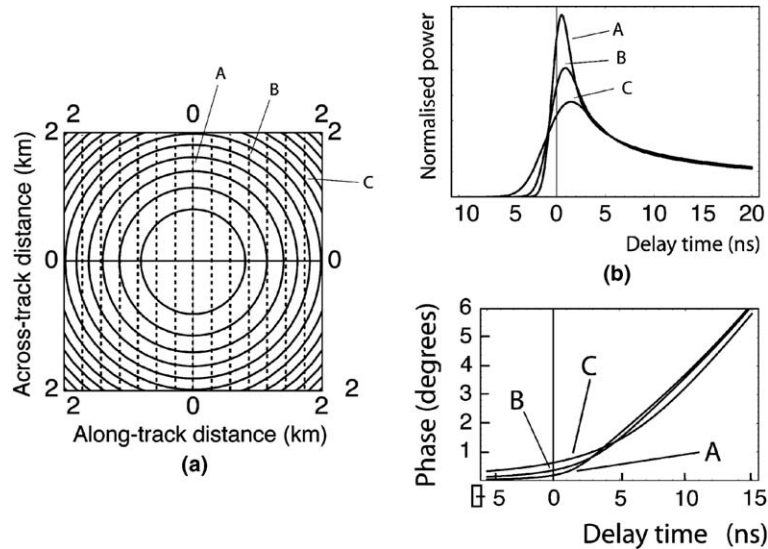
Fig. 11. (a): The relationship between the range rings from a surface with a constant gradient (solid lines) and the lines of maximum beam gain (dashed lines); (b): (upper panel) the mean echo power corresponding to the labelled beams in (a), and (lower panel) the mean echo phase departure.

dependence on the look angle. In fact, Fig. 11(a) illustrates the situation irrespective of the *direction* of the surface gradient. This illustrates that the echoes are less functions of look angle than of the angle the beam makes with the *along-track* surface gradient. For a beam striking the along-track gradient normally-beam 'A' in Fig. 11(a) is an example-the echo energy is largely concentrated in that emerging from the pulse-limited footprint. In this sense, the 'footprint' of the beam is approximately 300 m along-track by 1.5 km across-track. For beams striking the surface at an angle-beams 'B' and 'C'– are examples – the sharp, early return is less emphasised, and the echo somewhat more dispersed in delay time. In Eq. (14) a dependence on look angle can only occur due to the antenna gain. This is no longer the case once the effect of a finite beam width and pulse duration are allowed for. For the region shown in Fig. 11(a) the antenna gain has little variation. The variation in echo shape is due to the changing relationship, evident in Fig. 11(a), between the beam width and the range rings as the beam angle to the along-track gradient varies.

Turning to the phases shown in Fig. 11(b), the plot shows the departure of the phase from that associated with the POCA (that is, in Eq. (15), from $(k_0 B/\eta)\tan\beta$. The essentially linear dependence of Eq. (14) on delay for positive delay is apparent in the plot, but, in detail, the phase behaviour has a distinct curvature, and for no value of delay does it exactly equal $k_0 B/\eta)\tan\beta$.

These descriptions of the echo apply to 'smooth' surfaces whose gradient is less than that of the angles illuminated across-track by the antenna gain, that is surfaces whose gradient is less than 0.8°. This is generally not the case. If the across track gradient exceeds

the angles illuminated by the antenna gain, the echo changes markedly. In such a situation, the POCA is not illuminated, and the sharp leading edge of the echo will not be present. Second, only one of the two terms of Eq. (14) will have significant energy. In this case, the geometry is similar to that of sideways-looking radar, save that it is the surface that is tilted, rather than the antenna. The terms 'altimeter-like' and 'swath-like' are used to distinguish the two cases.

3.3. Determination of backscattering variation with incidence angle

Following the beam forming and slant range correction, the echoes from beams directed at a particular location $\mathbf{x}_s$ are gathered to form a 'stack'. The stack forms the set $\psi(\mathbf{x}_s, t_{sr}, \theta_l(i))$, $i \in \{1, N_L\}$. N_L, which is discussed further in Section 3.4, is the number of beams in the stack. If i has the order in which the bursts are observed, successive values of i correspond to approximately equal increments of incidence angle. The variation of echo power with incidence angle, illustrated in Fig. 12, results partly from variations of the surface backscattering coefficient. As Fig. 12(a) shows, over a uniformly rough surface, the maximum power occurs when beam incidence angle is normal to the along track gradient. However, if the surface scattering becomes specular, the spread of power with incidence angle will narrow considerably. Detecting this behaviour is important, at *level 2*, to distinguish the scattering of sea-ice floes and that of the intervening leads. To characterise the variation, the 'power stack' (i.e., $\psi\bar{\psi}(\mathbf{x}_s, t, \theta_l(i))$) is integrated over delay time and the estimated noise power subtracted. The mean, standard deviation, skew-
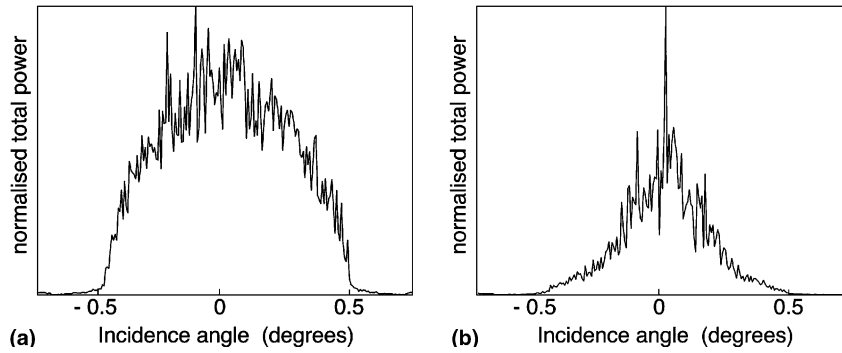
Fig. 12. Simulated variation of total echo power in SARM over: (a) a uniformly rough, spherical surface (e.g., the ocean), and (b) a surface with a marked specular component around zero incidence angle (e.g., a lead in sea ice). The fluctuations are the result of radar speckle.

ness and kurtosis of the resulting distribution (now considered only a function of i), illustrated in Fig. 12(b), are reported in the *level 1b* data product.

3.4. Multi-looking

Multi-looking describes the averaging of the stack power and cross product over the look angle to reduce the effects of the speckle. The multi-looked cross product is, for example,

$$\psi\bar{\psi}_{ml}^{(+,-)}(\mathbf{x}_s, t_{sl}) = \frac{1}{N_L} \sum_i \psi^{(+)}\bar{\psi}^{(-)}(\mathbf{x}_s, t_{sl}, \theta_l(i)). \tag{16}$$

Following this, the multi-looked power is written to the HBR *level 1b* product. In SARInM, the multi-looked power is the average of the multi-looked power at each antenna.

In SARInM, two additional functions are written to the product, the multi-looked phase:

$$\Delta_{ml}(\mathbf{x}_s, t_{sl}) = \text{Arg}(\psi\bar{\psi}_{ml}^{(+,-)}(\mathbf{x}_s, t_{sl})) \tag{17}$$

and the multi-looked coherence

$$K_{ml}(\mathbf{x}_s, t_{sl}) = \frac{|\psi\bar{\psi}_{ml}^{(+,-)}(\mathbf{x}_s, t_{sl})|}{\psi\bar{\psi}_{ml}(\mathbf{x}_s, t_{sl})}. \tag{18}$$

As Section 3.2 shows, the echoes in the stack, even following the slant range correction, have a dependence on look angle surface gradient. The multi-looked echo is an average over these dependencies. Fig. 13(a) shows examples of the mean multi-looked power for a surface with no gradient, and a surface with an along and across-track gradient. These may be compared with the individual echoes from the stack shown in Fig. 11(b). Notable features of the multi-looked echo are the reduced maximum in comparison with that from the beam normal to the surface, and the small sensitivity to the surface gradient. This limited sensitivity is quite remarkable, given the differences in along- and across-track illuminations. The most notable feature of the

multi-looked phase, Fig. 13(b), is the clear bias at zero delay time.

In general, N_L, the number of looks, varies slightly with the orbit and the surface, and its value too is written into the product. However, if one wishes to use this number to estimate the statistical fluctuations of the power, or, together with the coherence Eq. (18), those of the phase, a word of caution is needed. First, in SAR-InM, N_L should be doubled because the powers at the two antennas are largely uncorrelated. Second, the conventional expressions (see e.g., Jensen, 1999) for these fluctuations depend on the summations (of, for example, Eq. (16)) being over samples drawn from a population with the same mean. As Figs. 11(b) and 13 show, this is not the present case, because the means depend on the look angle. As a rough rule, the fluctuations of the power and phase are those provided by the conventional expressions if half the value N_L of is used. See Wingham et al. (2004) for details.

The multi-looked power, phase and coherence are written in the products as functions of $(\mathbf{x}_s, t_{sl} + 2z_0/c + n\Delta_t)$, $n \in \{-N_s/2, N_s/2 - 1\}$. Here, Δ_t is the delay-time sampling interval of 3.125 ns. The number of samples N_s is 128 for SARM, and 512 for SARInM. Finally, the units of power used in the product are Watts (W) referred to the antenna. In the processing, the summations of Eq. (16) are normalised such that the noise power is unaffected: the noise power appearing in the product is that of the pulse-limited, *level 0* echoes. This accounts for the factor of 1/8 that appears in Eq. (5).

3.5. LRM mode level 1b data

In LRM mode, the altimeter operates as a conventional, pulse-limited altimeter (see e.g., McGoogan, 1975). In LRM, as with earlier altimeters, the range compression and incoherent averaging are performed on board (Section 2.1) and the resulting averaged, pulse-limited echo forms the LRM *level 0* data. At *level 1b*, the echoes are instrument corrected and geo-located
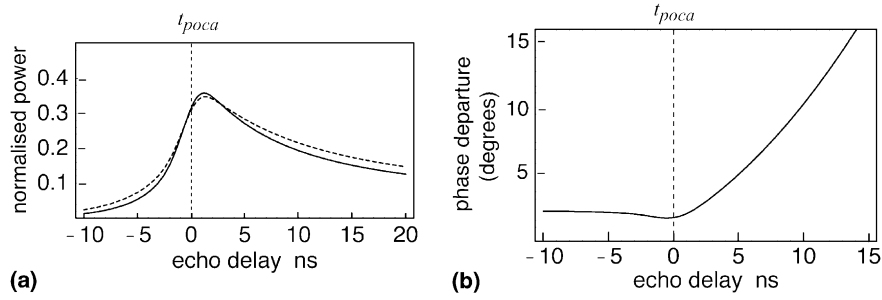
Fig. 13. (a) The multi-looked power from a uniformly scattering surface. Solid line: a sphere with a radius equal to that of the Earth; dashed line: a surface inclined to the sphere at 0.5° across-track. (b) The departure of the multi-looked phase from that of the point of closest approach (POCA) (from Wingham et al. 2004).

but are otherwise passed unchanged to the LRM *level 1b* data. The geo-location of the averaged echo is performed in a similar fashion to that of the HBR data (Section 3.1), save that the central burst location of the HBR data is replaced with the central location of the 91 'start–stop' locations corresponding to the individual LRM echoes.

While the theory of pulse-limited echoes from the inclined surface of Section 3.2, or, equivalently, a mis-pointed antenna, is well known (Brown, 1977; Hayne, 1980), one feature of the SIRAL LRM that differs from earlier pulse-limited systems is its elliptical antenna pattern (Section 3.1). In the general case of a mis-pointed antenna with an elliptical pattern, the rough surface impulse response can only be given as an integral. However, for a small mis-pointing angle α and a small ellipticity an asymptotic expansion provides

$$I(\tau) \sim \frac{\lambda^2 D_0 \sigma^0 G_0^2 c}{64\pi^2 z_0^3 \eta} \exp\left(-\left(\frac{\alpha^2}{\eta^2} + \frac{c\tau}{z_0\eta}\right)\left(\frac{1}{\gamma_2^2} + \frac{1}{\gamma_1^2}\right)\right)$$
$$\times \left(1 + \frac{\alpha^2 c\tau}{z_0\eta^3}\left(\frac{1}{\gamma_2^2} + \frac{1}{\gamma_1^2}\right)^2 + \frac{c^2\tau^2}{4z_0^2\eta^2}\left(\frac{1}{\gamma_2^2} - \frac{1}{\gamma_1^2}\right)^2\right)$$
$$(19)$$

for the pulse-limited, rough surface impulse response. To this order of approximation, the effect of mis-pointing is quadratic in α and linear in delay τ, the effect of the ellipticity quadratic in delay τ, and the azimuthal relation between the orientation of the antenna and

the direction of the surface gradient has no effect. Further details may be found in Wingham and Wallis (submitted).

4. CryoSat *level 2* data processing and products

The *level 1b* processing results, generally, in a sequence of radar echoes along the satellite track, one echo for each along-track location. In all of the modes, the locations are separated at approximately 300 m intervals along the track. The *level 2* processing is concerned, generally, with estimating from each echo a surface elevation (and other parameters such as surface backscatter).

The *level 2* product is a single, global product. On the other hand, while the 'geophysical' corrections are common to all three modes, the *level 2* processors themselves are mode dependent. This leads to the overall data flow shown in Fig. 14.

The retrieval of a surface elevation (or any other physical property) from the radar echo requires a model that relates the radar echo to the elevation (or other property). The models used in radar altimetry are simple, ignoring many detailed uncertainties of geometry and scattering behaviour. This is because, generally, more complicated models are undetermined by echo; different physical models may account for the same echo (see e.g., Wingham, 1995). Our approach is to process the data using simple models, knowing that 'model' errors may result, and use independent measurements to
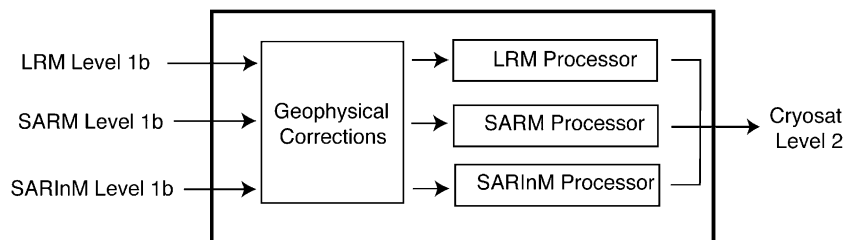

Fig. 14. Overview of CryoSat *level 2* processing.

verify that these are small, or can by changing the model be made small. In this section, the models are identified; potential sources of model errors are dealt with in Section 6.

4.1. SARInM level 2 processing

SARInM is operated over the marginal regions of the Earth's ice sheets and regions of mountain glaciers (Section 2.3). The model used for the elevation retrieval in SARInM is that of Section 3.2: we suppose the echo is scattered from a rough surface inclined at an angle to a sphere with a radius similar to that of the Earth. For such a surface, the point of closest approach in the across track plane containing the sample point x_s is unique. Let x_{sat} and x_{poca} denote the positions of the satellite and POCA in the plane, and let x_{poca} lie at a range r_{poca} in the direction $\hat{n}_{poca}$, so that

$$x_{poca} = x_{sat} + r_{poca}\hat{n}_{poca}. \tag{20}$$

If $\hat{n}_{poca}$ makes an angle $\pi/2 - \rho_{poca}$ with the interferometer baseline $\hat{m}_b$, $\hat{n}_{poca}$ satisfies the simultaneous equations

$$|\hat{n}_{poca}| = 1 \qquad \hat{n}_{poca} \cdot \hat{n}_2 = 0 \qquad \hat{m}_b \cdot \hat{n}_{poca} = \sin \rho_{poca}. \tag{21}$$

With x_{sat} and $\hat{n}_2$ known from the orbit determination, $\hat{m}_b$ from the star-tracker measurement, r_{poca} from the leading edge of the echo power and $\sin \rho_{poca}$ from the interferometric phase, Eq. (21) determine the direction $\hat{n}_{poca}$. (In fact, Eq. (21) have two solutions, but one of these lies above the satellite, and may be discarded.) x_{poca} is then determined from (20). The elevation is then simply the 'vertical' coordinate z_{ice} of the vector x_{poca} when described in the ellipsoidal WGS system.

The measurements of x_{sat}, $\hat{n}_2$ and $\hat{m}_b$ are determined by the *level 1b* processor, and the main task of the *level 2* processor is the estimation of the range r_{poca} and the interferometric phase. This process is termed, for historical reasons, 'retracking'. In outline, the process is simple. The function $f_\psi(\tau - \tau_0, \alpha_i)$ is taken to describe the theoretical shape of the mean, multi-looked echo. τ_0 is the time corresponding to the arrival from the POCA. The α_i are parameters that define other aspects of the shape. The values of τ_0 and α_i are varied so as to minimise in the least squares sense the difference between $f_\psi(\tau - \tau_0, \alpha_i)$ and the measured multi-looked echo. With τ_0 thus determined, the range to the closest approach is determined from

$$r_{poca} = z_0 + c\tau_0/2. \tag{22}$$

In practice, the choice of $f_\psi(\tau, \alpha_i)$ is not altogether obvious. This is because the measured echoes will depart from the theoretical echoes as a result of (at least) unknown topographic variations. $f_\psi(\tau, \alpha_i)$ has to be chosen so as to closely coincide with the theoretical echo when the surface conforms to the model (which includes, for example, the ocean surface), whilst adapting in a 'sensible' fashion as the measured echoes depart from the modelled echoes. There is no unique choice. The function we have chosen has six parameters, and is based on 'stretching' the argument of a Gaussian function so as to make it coincide (very closely) with theoretical echoes. Its precise form is given in Appendix A. Fig. 15(a) illustrates the meaning of the six parameters, Fig. 15(b) illustrates the fit to a simulated echo.

To determine the phase, we minimise the functional

$$\frac{K_{ml}^3(x_s, t_{sl})}{1 - K_{ml}(x_s, t_{sl})} \left| \exp[i(\text{Arg}(\psi^{(+)}\bar{\psi}^{(-)}(\tau, \theta_l)) - g(\tau, \chi_i))] \right|^2 \tag{23}$$

with respect to the parameters χ_i, where the function $g(\tau, \chi_i)$ has the form

$$g(\tau, \chi_i) = \begin{cases} \chi_1 & \tau < \tau_0, \\ \chi_1 + \chi_1(\tau - \tau_0) & \tau > \tau_0 \end{cases} \tag{24}$$

suggested by Eq. (15). The weighting by the leading function of coherence provides a maximum likelihood estimate (Jensen, 1999). χ_1 is the estimate of the phase of the POCA, χ_2 its slope for $\tau > \tau_0$. In minimising Eq. (23), τ_0 is not a variable, but is equal to the value determined from the range retracking. With χ_1 determined, one then uses

$$\sin(\rho_{poca} + \varepsilon_\rho) = \chi_1/k_0 B \tag{25}$$

to estimate in turn $\hat{n}_{poca}$ using Eq. (21). Here, ε_ρ accounts for any error arising in using the interferometric phase to estimate $\sin \rho_{poca}$. An example of a fit of to a simulated echo is shown in Fig. 15(c); the corresponding weights in 15(d).

The complete processing chain is illustrated in Fig. 16. Eqs. (20) and (21) are implemented within the section labelled 'elevation determination', while the functional fitting is performed within the 'range and phase retracking' section. There are, in addition, two other elements to the processing chain. The elevation presupposes that the POCA lies within the across-track angles illuminated by the antenna, i.e., the echo is 'altimeter-like' (see Section 3.2). The range of angles is limited to ~1° of the nadir direction (see Fig. 4(a)). The processor will also encounter 'swath-like' echoes in the ice sheet margins and smaller, temperate ice bodies. Elevation retrieval is certainly possible for such echoes (the method is that of SAR interferometry) but the precision is likely to be too poor for useful ice sheet change measurements. The *level 2* processor is designed to deal solely with 'altimeter-like' echoes. The first stage of the processor, illustrated in Fig. 16, is to provide 'leading edge discrimination' of echoes with a sharp leading edge, suitable for the POCA retrieval. If the discriminator fails to find a
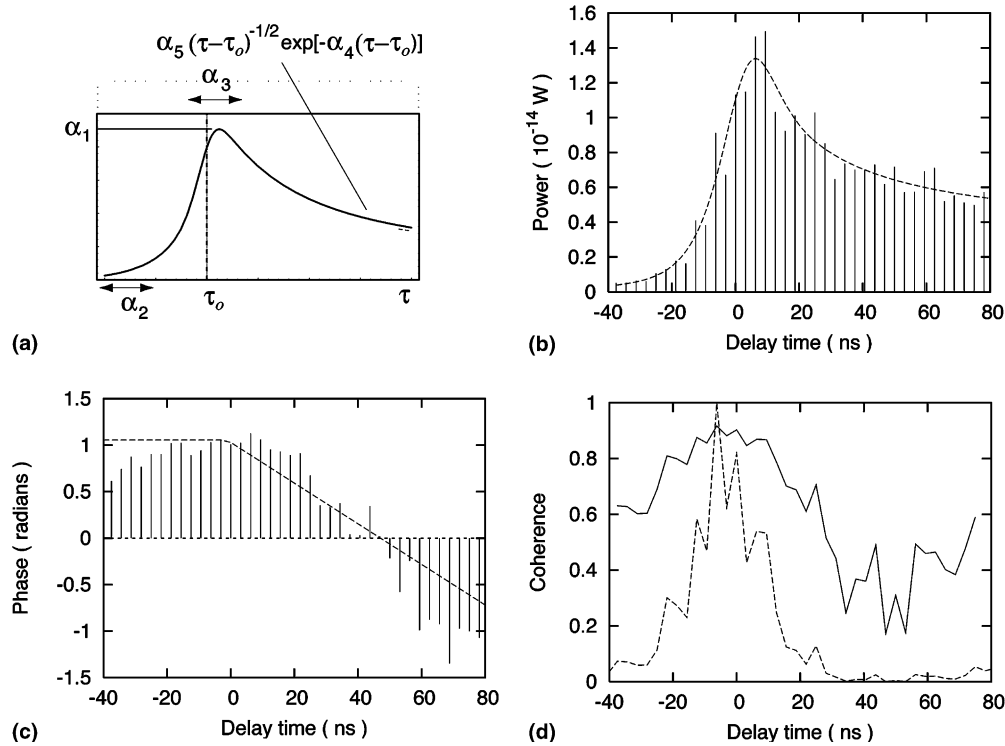
Fig. 15. (a) The function $f(\tau, \alpha_i)$ used to determine the arrival time of the POCA. τ_0 is the arrival time of the POCA; α_1 is the maximum power. α_2 measures the duration of the leading edge 'toe'. α_3 is the duration of the peak; it can adapt in particular to varying surface roughness. α_4 describes the contribution of the antenna pattern to the echo trailing edge, and α_5 controls its amplitude; the functional combination of these parameters is suggested by (3.13); (b) a fit of $f(\tau, \alpha_i)$ to a simulated, multi-looked echo power, with parameter values $\alpha_1 = 1.33 \times 10^{-14}$ W, $\alpha_2 = 80.4$ ns, $\alpha_3 = 14.4$ ns, $\alpha_4 = 5.88 \times 10^{-4}$ ns^{-1} and $\alpha_5 = 2.65 \times 10^{-14}$ W; (c) a fit of $g(\tau, \chi_i)$ to the corresponding simulated, multi-looked phase with parameter values $\chi_1 = 60.5°$ and $\chi_2 = 1.25°$ ns^{-1} and (d) the simulated coherence (solid line) and weights (dashed line) used in the phase fitting.
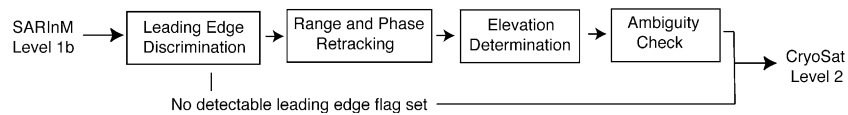

Fig. 16. The *level 2* SARInM processing chain.

leading edge, a flag is set, and further elevation processing discontinued.

The final element of the chain recognises the possibility that mis-ranging may occur if energy from an ambiguous beam (Section 3.1) is misinterpreted as the earliest echo arrival, or if the across-track angle is misinterpreted as a result of wrapping of the interferometer phase. In either case the elevation error that results is of the order of 100 m. The 'ambiguity check' compares the measured elevation with an elevation model of the surface, and flags the value if it exceeds the model value by 50 m.

4.2. SARM level 2 processing

SARM is operated over regions of the Earth's sea-ice (Section 2.3). The *level 2* processing aims to provide the elevation of the ice or the ocean elevation, together with the ice freeboard, i.e., the elevation of the ice above the local sea-level. The model used for the retrieval of sea-ice thickness is shown in Fig. 17(a). Laboratory experiments (Beaven, 1995) and comparisons with in situ thickness observations (Laxon et al., 2003) show that when snow is present on the ice, the radar ranges to the snow–ice, rather than the air–snow, interface, and the freeboard is then the difference between the measured ice elevation and the local sea-level.

Over sea-ice, it is assumed the leading edge of the echo is scattered from the surface at in the nadir direction. The instantaneous elevations of the ice z_{ice} and ocean z_{ocean} are determined using Eq. (20) with $\hat{\mathbf{n}}_{poca} = \hat{\mathbf{n}}_n$ and the ranges determined using Eq. (22) and a retracker in a manner similar to that for the SAR-InM. The derivation of the freeboard is less straightforward. Observations of the ocean are available only at breaks – leads in the ice cover. Between the leads, the local sea-level may vary considerably, mainly as a result of the geoid and dynamic topography variations
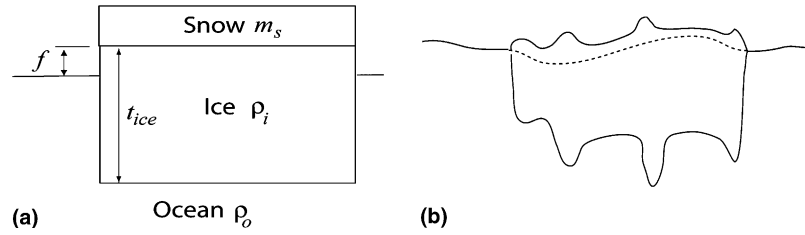
Fig. 17. (a) The model used to determine ice freeboard f and thickness t_{ice}; (b) an illustration of how sea level fluctuation may effect the ellipsoidal ice elevation within an ice flow and between successive observations of the sea surface.

(Fig. 17(b)). For this reason, the freeboard is estimated using

$$f_{est}(\mathbf{y}, t) = z_{ice}(\mathbf{y}, t) - z_{mean}(\mathbf{y}) - \sum_j \Omega_{ocean}(\mathbf{y}, \mathbf{y}_j)$$
$$\times (z_{ocean}(\mathbf{y}_j, t) - z_{mean}(\mathbf{y}_j)). \tag{26}$$

Here $\mathbf{y}$ is a position vector indicating a point on the ellipsoid, and t is elapsed (calendar) time. z_{mean} is the mean sea-surface, assumed known. Ω_{ocean} is a filter that acts on elevations $z_{ocean}(\mathbf{y}_j)$ in the vicinity of $\mathbf{y}$ and observed from the same orbit as $z_{ice}(\mathbf{y})$. Because the satellite speed is large compared with motions of the ice or ocean, all the measurements in Eq. (26) may then be treated as occurring at the same instant t.

Within the *level 2* processor, Ω_{ocean} extends over 100 km and has uniform weights. In Eq. (26), the mean sea-surface is subtracted from the ice and ocean elevations; what remains are anomalies from the mean sea-surface. These, apart from the freeboard itself, are due to tides and variable dynamic topography. By assumption, these latter have a spatial scale that is large in comparison with the extent of the filter Ω_{ocean} and unaffected by it. Eq. (26) then removes from the ice elevations the component due to the time-variations in the local sea-level.

The complete processing chain is illustrated in Fig. 18. The approach to measuring the freeboard requires two passes of the data, the first to determine the ice and ocean elevations, the second to form anomalies, smooth the ocean anomalies, and then subtract the result from the ice elevation to determine the freeboard. Prior to any of these, however, is the discrimination of ice and ocean echoes. This is done in part using the shape and power of the echo, and in part using the directional information available from the stacks (Section 3.4). The design also anticipates that it will not always be possible to distinguish the surface from the echo behaviour. In this case, a flag is set, and further processing is not performed.

4.3. LRM level 2 processing

The LRM is used over the central areas of the ice sheets, and the ice-free ocean (Section 2.3). In this mode,

the instrument operates as a conventional, pulse-limited altimeter (Section 2.1), and the processing is that of conventional, pulse-limited altimetry. The processing chain is similar to that of the ENVISAT radar altimeter, save for the addition of the ellipticity 'correction' given by Eq. (19). Further details may be found in the ENVISAT handbook (Benveniste, 2002).

4.4. Geophysical corrections

'Geophysical' corrections are made in the *level 2* data for the variation of the speed of the transmitted carrier wave through the atmosphere, and for tidal variations in the surface elevation whose presence in the data would otherwise confuse their interpretation. Table 2 lists the corrections applied to the CryoSat data, together with the specific source of the correction. These corrections are common to all radar altimeter missions, and are well known. Specific details on individual corrections are given in the references in Table 2. Also included in the table are typical magnitudes of the corrections at 80° N when averaged over one month and 10^4 km², determined empirically from ENVISAT RA-2 data.

5. Higher-level products

The primary goals of the CryoSat mission are to determine fluctuations in sea-ice and ice sheet thickness and mass averaged over various areas and time-intervals. If we take w as a generic quantity, the averages of main interest are

$$\hat{w} = \frac{1}{AT_d} \int \int_{Region} dA \int_{Interval} dt w(\mathbf{y}, t) \tag{27}$$

over a *Region* of area A and an *Interval* of duration T_d. The *Region* might be, for example, a drainage basin, and the interval might be the mission lifetime. The term 'higher-level product' is a short hand for the estimation of any of these averages from the *level 2* measurements.

The *level 2* data are, in space and time, point data, and there is a scale below which a useful average is not available (or, more precisely, requires a good deal of a priori information concerning the fluctuation
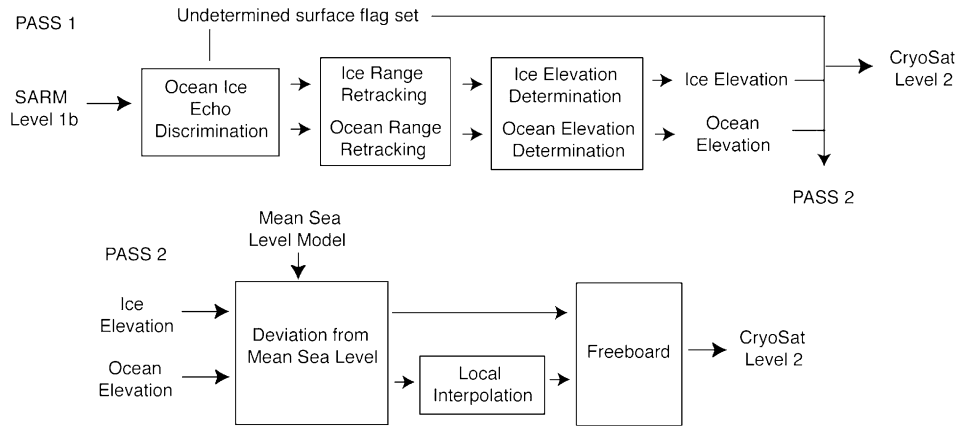
Fig. 18. The *level 2* SARM processing chain.

Table 2
Nature and source of geophysical corrections

Correction	Source	Typical winter magnitude at 80°N, averaged over 1 month and 10^4 km².	Reference
Ocean tide	FES 02	0.03 m	Le Provost et al. (1998)
Ocean loading tide	FES 02	0.002 m	Francis and Mazzega (1990)
Long-period tide	FES 02	0.0075 m	Le Provost et al. (1998)
Solid Earth	Cartwright Edden	0.015 m	Cartwright and Edden (1973)
Polar tide	Wahr	0.0025 m	Wahr, 1985
Dry troposphere	Meteo France/ECMWF	2.3 m ±0.02 m	Saastamoinen, 1972
Inverse barometric correction	Meteo France/ECMWF	0.03 m	Ponte (1991)
Wet troposphere	Meteo France/ECMWF	0.01 m	Saastamoinen (1972)
Ionosphere	Bent model	0.015 m	Llewwllyn and Bent (1973)

between the point samples). The starting point for any higher-level product is therefore to write Eq. (27) in the form

$$\hat{w} = \frac{1}{\sum_i \tau_i \sum_j A_j} \sum_i \sum_j \bar{\bar{w}}_{ij} \tau_i A_j, \qquad (28)$$

where $\bar{\bar{w}}_{ij}$ is the *local* average over a sub-region $\Re_j$ and sub-interval $\Im_i$. Typically, A_j may be the area of a sub-region $1° \times 1°$ in longitude and latitude, and τ_i the duration of an orbit repeat cycle, or sub-cycle, which, in the case of CryoSat, is 30 days.

The sub-domains are small, and it is sometimes notationally convenient at least to ignore the fact that the local average is a discrete function, and treat it as if it were a continuous function of space or time. Thus we may write, for example, $\bar{\bar{w}}_j(t)$ where t is a time representative of the sub-interval $\Im$. One is also interested in solely spatial averages over the *Region*, which we will denote $\hat{w}(t)$.

In practice, the procedures that generate higher-level products may vary depending on the particular problem, the form of the data themselves (for example, the presence or not in the data of an annual cycle) and to an extent the investigator. Nonetheless, the procedures are essentially similar, and those described in this section may be taken as a reasonable proxy for all of them.

5.1. Trends in ice sheet elevation and mass

Over the ice sheets, the principal scientific concern is with changes of mass, rather than elevation, and we consider first the relationship between these variables. In an area of mass accumulation, which describes the majority of the Antarctic and Greenland ice sheets, the elevation trend arises from the balance between the mass per unit area $\dot{m}_s$ arriving as snowfall and the column mass per unit area $\dot{m}_f$ leaving by flow. The relationship between these variables and the elevation rate is not straightforward as a consequence of the densification of the firn in the near surface (Arthern and Wingham, 1998). At its simplest (Wingham, 2000), the instantaneous elevation change is

$$\dot{h}_{ice}(\mathbf{y}, t) = -\frac{\dot{m}_f(\mathbf{y}, t)}{\rho_{ice}} + \int_0^\infty d\tau \dot{m}_s(\mathbf{y}, \tau) D(\mathbf{y}, t - \tau), \qquad (29)$$

where the densification kernel D depends on the local conditions. (We ignore here the distinction between ellipsoidal elevation change and ice thickness change arising due to basal melting or isostatic rebound.) In general, the contribution of the surface mass balance $\dot{m}_s$ to the trend depends on its temporal and spatial correlation scale in comparison with respectively the interval T_d and the area A.

In the interior of ice sheets at least, a reasonable model for the fluctuation in surface balance is $\dot{m}_s(\mathbf{y}, t) = \dot{m}_0(\mathbf{y}) + \dot{m}_1(\mathbf{y}, t)$, where $\dot{m}_0(\mathbf{y})$ may be regarded as, for example, the century mean, and $\dot{m}_1(\mathbf{y}, t)$ has a standard deviation of σ_m and correlation scales τ_m and A_m. Typical scales in practice are $\sigma_m \sim 0.25 \dot{m}_0$, $\tau_m \sim 1$ year and $A_m \sim 10^5$ km^2. If the measurement interval is short compared with the temporal duration of $D(\mathbf{y}, t)$ (typically 30 years), and the measurement interval and area large in comparison with the correlation scales, one has that, approximately

$$\hat{\dot{m}}_0 - \hat{\dot{m}}_f = \rho_{ice}\hat{\dot{h}} - \frac{\rho_{ice}}{\rho_{snow}}\hat{\dot{m}}_1, \tag{30}$$

where $\hat{\dot{m}}_1$ has a standard deviation of $\sigma_m \sqrt{(t_e - t_s)A/(\tau_m A_m)}$. The equation shows that care is needed in interpreting short elevation time series. While its standard deviation and correlation scales are reasonably established (see e.g., Wingham, 2000), $\dot{m}_1(\mathbf{y}, t)$ itself is not usually known, and the second term of Eq. (30) has to be regarded as an error if one is interested in, for example, the century-scale imbalance.

Turning now to the estimation of the average elevation rate, one has directly from the definition Eq. (27) that

$$\hat{\dot{h}}(t, t_s) = \frac{1}{t - t_s}(\hat{h}(t) - \hat{h}(t_s))$$
$$= \frac{1}{t - t_s}(\hat{h}(t) - \hat{h}(t_1) - (\hat{h}(t_s) - \hat{h}(t_1))), \tag{31}$$

where t and t_s are the start and end of the temporal averaging period, and we will think of t_s as a fixed parameter and t as a varying. The first line of Eq. (31) merely states that the average elevation rate equals the elevation change over the interval divided by its duration. The purpose of the second line, which introduces the apparently redundant parameter t_1, also regarded as fixed, will become clear shortly.

As noted in the introduction to this section, the processing aims to form the local averages of $h(t) - h(t_1)$. Again by definition, one has for the continuous quantity h that

$$\int\int_{\Re_j} dA \int_{\Im_i} dt h(\mathbf{y}, t) - \int\int_{\Re_j} dA \int_{\Im_k} dt h(\mathbf{y}, t)$$
$$= \int\int_{\Re_j} dA \left(\int_{\Im_i} dt h(\mathbf{y}, t) - \int_{\Im_k} dt h(\mathbf{y}, t) \right). \tag{32}$$

These are identities for a continuous function, but the same is not true when considering using the irregularly sampled, point data $z_{ice}(\mathbf{y}(t_j), t_j)$ to approximate in practice either expression. The left equation describes taking the temporal difference (from $\Im_k$ to $\Im_i$) of spatial averages; the right hand spatially averaging temporal differences *at the same location*. Experience shows that the former has a result that is dominated by errors in the

spatial integration. Therefore it is the right-hand-side equation is approximated, by reducing the measured elevations involved to the set of data occurring at crossing points of the orbit, that is, to the set of points at which

$$\mathbf{y}(t_i) = \mathbf{y}(t_j) \quad i \neq j. \tag{33}$$

This set may be further subdivided into two sets according to whether the later orbit is ascending or descending. These two sets are denoted by $\delta_{i,j}^{a-d}$ and $\delta_{i,j}^{d-a}$. Elevation changes are determined at such crossing points by forming *cross-overs*,

$$\Lambda_{a-d}(\mathbf{y}_i, t_i, t_j) = \delta_{i,j}^{a-d}(z_{ice}(\mathbf{y}(t_i), t_i) - z_{ice}(\mathbf{y}(t_j), t_j)) \tag{34}$$

for example, and local averages are formed using

$$\bar{\bar{\Lambda}}_k(t, t_1) = \sum_{i \cdot j} \Omega_{kij}^{(a-d)}(t, t_1)\Lambda_{a-d}(t_i, t_j)$$
$$+ \sum_{l,m} \Omega_{klm}^{(d-a)}(t, t_1)\Lambda_{d-a}(t_1, t_m). \tag{35}$$

The filters Ω define the sub-region $\Re_k$ and the two sub-intervals $\Im_t$ and $\Im_{t_1}$. One then takes

$$\bar{\bar{h}}_k(t) - \bar{\bar{h}}_k(t_s) = \bar{\bar{\Lambda}}_k(\mathbf{y}, t, t_1) - \bar{\bar{\Lambda}}_k(\mathbf{y}, t_s, t_1) + \varepsilon_k(t, t_s, t_1) \tag{36}$$

from which $\hat{\dot{h}}$ may be estimated using Eq. (31).

The introduction in Eq. (35) of separate filters for later ascending or descending orbits ensures that errors that are functions of space and satellite direction only (such as, for example, 'geographically-correlated' orbit error) are cancelled even when the numbers in the two sets differ (for various practical reasons). The procedure was introduced by Zwally et al. (1989) and has been used, essentially unchanged, by all succeeding investigators.

In Eq. (36), the 'redundant' parameter t_1 may be taken to label any sub-interval lying between t_s and t. Orbit repeat to orbit repeat, the cross-overs do not lie at exactly the same locations, and the error $\varepsilon_k(t, t_s, t_1)$, particularly the contribution of the speckle error, will decorrelate to an extent if different values of t_1 are selected. Thus, the right-hand side Eq. (36) may be replaced by an average over values of t_1 to reduce the contribution of the speckle-error to $\hat{\dot{h}}$.

There is a second practical point in connection with Eq. (36). It is open to the objection that it uses only the end points of the time series $\bar{\bar{\Lambda}}_k(t, t_1)$; it does not make use of the intervening values. In practice, the right-hand-side of Eq. (36) is often replaced with the gradient of a linear (or more sophisticated) fit to $\bar{\bar{\Lambda}}_k(t, t_1)$. It is true that this reduces the measurement error, but one is left with the problem (invariably ignored) of ascribing a precise *physical* meaning to the gradient – see Fig. 19 for an example.

Recently, it has become clear that the error $\varepsilon_k(t, t_s, t_1)$ of Eq. (36) contains a term arising from temporal varia-
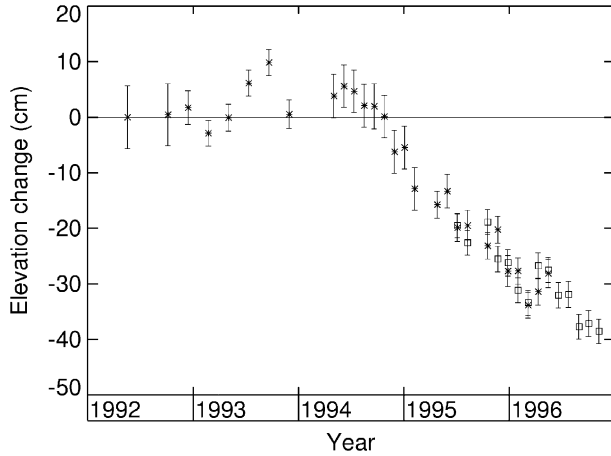
Fig. 19. The time series $\hat{\Lambda}_k(t, t_1)$ for the Thwaites and Pine Island glaciers basins, West Antarctica, measured by the ERS altimeters. In this case, $t_1 =$ April 1993. The estimated change in elevation value for the interval from $t_s =$ April 1992 to $t =$ December 1996 is -38 ± 7 cm or a average elevation rate of -8.14 ± 1.5 cm yr^{-1}. The contribution of the measurement error to a fitted linear trend is only 0.13 cm yr^{-1}; but the physical meaning of the trend is unclear (from Wingham et al., 1998).

tions in the scattering properties of the firn. In broad terms, the volume scattering contribution to an ice sheet altimeter echo is understood (see, for example, Ridley and Partington, 1988; Haardeng-Pedersen et al., 1998): the scattering cross-section decays exponentially into the firn, with a penetration depth of a few metres, and, typically, the total energy of the surface and volume contributions are approximately equal. The effect of adding a volume contribution to the mean echoes of Fig. 13 is shown in Fig. 20(a). Were the two contributions to bear a fixed relation to the physical surface, any error introduced would be cancelled by the differencing of Eq. (34). However, this does not happen in practice. One effect, which is clearly established (Arthern et al., 2001), arises because the surface backscatter coefficient varies as a result of meteorological processes. Changing the ratio of surface to volume scattering alters

the echo shape, and an error in the measured elevation results. The 'tell-tale' of this error is that changes in surface backscatter change the total echo energy, and the result is correlated fluctuations in power and measured elevation (Fig. 20(b)).

The effect may be corrected by determining, from the measurements, a correlation coefficient $k_p(\mathbf{y})$ between energy and elevation change (Wingham et al., 1998). The coefficient must be determined from correlations that are local in time, to prevent the signal trend being removed from the data, and local in space, because the coefficient depends on the ratio of the surface to the volume energies. One also forms, in addition, energy crossovers $\bar{\bar{\Theta}}_k(\mathbf{y}, t, t_1)$ in an exactly analogous fashion to Eqs. (34) and (35), and replaces Eq. (36) with

$$\bar{\bar{h}}_k(t) - \bar{\bar{h}}_k(t_s) = \bar{\bar{\Lambda}}_k(\mathbf{y}, t, t_1) - \bar{\bar{\Lambda}}_k(\mathbf{y}, t_s, t_1) - k_p(\mathbf{y})(\bar{\bar{\Theta}}_k(\mathbf{y}, t, t_1)$$
$$- \bar{\bar{\Theta}}_k(\mathbf{y}, t_s, t_1)) + \varepsilon_{k1}(t, t_s, t_1). \quad (37)$$

While the fluctuations illustrated in Fig. 20(b) are those associated with a pulse-limited system, the physical effect-the temporal change in surface backscatter in the presence of largely unchanged volume scatter-will occur too in the case of SIRAL echoes. On the other hand, the sensitivity of the SIRAL echo to the surface and volume components illustrated in Fig. 20(a) are different from those of a pulse-limited echo (Ridley and Partington, 1988). The coefficient $k_p(\mathbf{y})$ in Eq. (37) will need to be evaluated anew for the SIRAL echoes.

5.2. A really averaged sea-ice thickness and mass

In any local subregion $\Re_j$ of sea-ice covered ocean of area A_j falling within the subinterval $\Im_i$, one may construct a cumulative area-interval function A_c of ice thickness t_{ice} such that its value is the area-interval 'volume' of sea-ice whose thickness is less than t_{ice}. One may then define a sea-ice thickness density function

$$\bar{\bar{p}}_i(t_{ice}) = \frac{1}{V_{ice}} \frac{dA_c(t_{ice})}{dt_{ice}}, \quad (38)$$
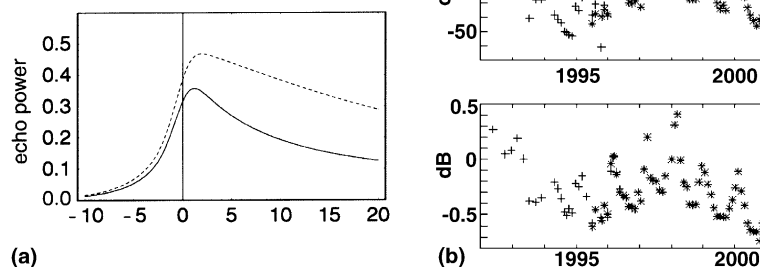

Fig. 20. (a) The effect on the SIRAL echo of adding a volume scattering contribution (dashed) to the echo with only a surface contribution (solid line); (b) correlated fluctuations in measured elevation change (top) and echo power (bottom) as observed by the ERS-1 (crosses) and ERS-2 (stars) altimeters in a 10^4 km^2 vicinity of 80°S, 50°E in East Antarctica.

where V_{ice} is the total area-interval 'volume' of sea-ice within the area. One may also construct a second density function

$$\bar{\bar{p}}_{i+w}(t_{\text{ice}}) = (1 - C_{\text{ice}})\delta(0) + C_{\text{ice}}\bar{\bar{p}}_i(t_{\text{ice}}) \quad (39)$$

where $C_{\text{ice}} = V_{\text{ice}}/A\tau_a$ is the average ice concentration. Eq. (39) treats open water as ice of zero thickness. The mean ice volume per unit area of ocean surface is then

$$\bar{\bar{t}}_{\text{ice}} = \int_0^\infty dt_{\text{ice}} t_{\text{ice}} \bar{\bar{p}}_{i+w}(t_{\text{ice}}) = C_{\text{ice}} \int_0^\infty dt_{\text{ice}} t_{\text{ice}} \bar{\bar{p}}_i(t_{\text{ice}}) \quad (40)$$

where the first equation follows (not quite directly) by definition from Eq. (27) with Eq. (38), and the second equation from Eq. (39). The definitions Eqs. (38) and (39) make no claim on random variable theory although Eq. (38) is consistent with regarding the density functions that way if it is useful. The choice of density function depends on the problem under consideration; $\bar{\bar{t}}_{\text{ice}}$, for example, is the quantity that usually appears in numerical climate models. Averages over larger areas then follow using Eq. (28).

The satellite measurements are made with a finite resolution of approximately 1 km × 250 m. Thus, while we have defined $\bar{\bar{p}}_i$ as that of the thickness at a point, the measurements will smooth the thickness distribution on the scale of the resolution, and $\bar{\bar{p}}_i$ will in fact be the density function at this resolution. To the extent the smoothing is linear, $\bar{\bar{t}}_{\text{ice}}$ is unaffected by it. However, the smoothing needs to be accounted for in comparing the satellite measurements of the density function with measurements from sensors with a higher resolution.

To estimate the density functions, the thickness needs estimating from the estimated freeboard. To date, this has been done using the model of Fig. 17(a) and the assumption of hydrostatic equilibrium:

$$t_{\text{est}} = \frac{1}{\rho_{\text{ocean}} - \rho_{\text{ice}}}(\rho_{\text{ocean}}f_{\text{est}} + m_s). \quad (41)$$

Ocean and ice densities have been taken as the constants $\rho_{\text{ocean}} = 1022.9 \text{ kg m}^{-3}$ and $\rho_{\text{ice}} = 915.1 \text{ kg m}^{-3}$ respectively (Laxon et al., 2003), and the snow load from measured climatology (Warren et al., 1999). Sea ice mass per unit area may also be estimated as $\rho_{\text{ice}}t_{\text{est}}$.

Turning now to the formation of the local average, there will be within $\Re_j$ and $\Im_i$ N_{ice} observations of ice and N_{ocean} of ocean, together with a remaining set that are ambiguous and therefore unclassified. In detail, the relationship between the continuous average of Eq. (38) and that formed from the irregular samples of the measurements may be complex. However, past experience shows two general behaviours. First, the ratio $N_{\text{ice}}/(N_{\text{ice}} + N_{\text{ocean}})$ is a poor estimate of the average concentration because the probability of obtaining an unambiguous echo from the ocean is larger than that from the ice as a consequence of their differing backscatters. On the other hand, on the assumption that the N_{ice}
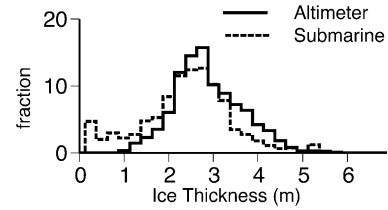

Fig. 21. Ice thickness density function $\hat{p}_i(t_{\text{ice}})$ estimated using ERS-2 altimeter measurements in the Beaufort Sea, October 1996 compared with that obtained from submarine upward-looking sonar (ULS) measurements over the same region and interval. The ULS measurements have been smoothed to the resolution of the radar. Ignoring sampling errors (termed 'higher-level' errors in Section 7) in the ULS measurement, it appears that the sampling of $\hat{p}_i(t_{\text{ice}})$ by the altimeter is not uniform: the ERS altimeters were insensitive to thin, presumably first-year, ice.

observations sample the ice density function uniformly, the distribution function of ice observations may be used as an estimate of A_c and/or $\bar{p}_i$ (see Fig. 21). The mean volume per unit surface area, for example, may then be obtained using Eq. (40) with an estimate of concentration obtained, for example, from passive microwave observations. This sampling distinction is why we introduce the two density functions of Eqs. (38) and (39).

Secondly, the backscatter coefficient of sea-ice is sensitive to the presence of meltwater. With the onset of melt, it is no longer possible to distinguish the ice from the ocean on the basis of the power in the echo; with the formation of meltponds the scatter from the ice is indistinguishable from that from the leads. Measurements are therefore unavailable during the melt season, restricting the observations in the Arctic to September to April.

6. Error budget and its validation

Errors that arise from the CryoSat measurements may be conveniently classified into one of three kinds. There are those that arise from the measurement system itself. The fluctuation arising from radar speckle seen in Fig. 15(b) and (c) is an example. They are present in the *level 1b* data and conveniently designated *level 1b* errors ε_{1b}. Second, errors arise because the models, such as that of Fig. 17(a), that are used to transform the point measured radar data to point 'geophysical' quantities, such as elevation, do not coincide with the actual situation. These arise in the *level 2* processing and we denote them ε_2, but it should be noted that some errors of this class, such as that arising in the calculation Eq. (41) of sea-ice thickness, are not present in the *level 2* products. Finally, errors ε_{hl} arise in higher-level products when forming local averages due to the sampling. ε_{1b} and ε_2 describe errors of commission; ε_{hl} those of omission.

In terms of these errors, the error that arises in the generic higher-level product $\hat{\hat{w}}$ is

$$\varepsilon_{\hat{\hat{w}}} = L_{\text{hl}}^{(\text{w})}(\varepsilon_2^{(\text{w})} + L_2^{(\text{w})}\varepsilon_{1\text{b}}) + \varepsilon_{\text{hl}}^{(\text{w})} \qquad (42)$$

where L_2 and L_{hl} denote the *level 2* and higher-level processes applied to the *level 1b* data. While it is common to characterise the errors of a satellite altimeter by describing the contributions (the 'budget') to the elevation error $\varepsilon_2^{(\text{h})} + L_2^{(\text{h})}\varepsilon_{1\text{b}}$, Eq. (42) shows that, for CryoSat, this may be misleading. First, the primary mission products are average elevation *rate* and sea-ice thickness. In both cases there is significant cancellation of elevation errors: Eq. (34) of the process $L_{\text{hl}}^{(\hat{h})}$ cancels time-invariant elevation errors, particularly those arising from ice sheet unknown topography, and Eq. (26) of $L_2^{(t_{\text{ice}})}$ cancels errors with a long-spatial scale, such as orbit or tidal errors.

Second, the processes L_{hl} spatially and temporally integrate the local averages. In consequence, the mean square error $E\{\varepsilon_{\hat{\hat{w}}}^2\}$ in a higher-level product is

$$E\{\varepsilon_{\hat{\hat{w}}}^2\} = \frac{1}{A^2 T_{\text{d}}^2} \int\int_{\text{Region}} \mathrm{d}A \int\int_{\text{Region}} \mathrm{d}A' \int_{\text{Interval}} \mathrm{d}t$$
$$\times \int_{\text{Interval}} \mathrm{d}t' E\{\varepsilon_{\bar{\bar{w}}}(\mathbf{y}, t)\varepsilon_{\bar{\bar{w}}}(\mathbf{y}', \mathbf{t}')\}, \qquad (43)$$

where $E\{\cdot\}$ denotes expectation, and we treat the local averages as continuous functions. Eq. (43) shows that it is that co-variance, and not the variance of the error in the local averages that determines the final error. The practical significance of this is that errors that may dominate the point elevation error budget may be negligible in the higher-level product; conversely, errors that dominate the higher-level budget may be insignificant (and even practically unobservable) in a point-measurement.

It is not possible within the scope of an article such as this to provide a complete breakdown of the errors, or to do justice to the wide range of experiments that may be performed to validate them. In this section, we summarise what is known of the errors with the aim of identifying the most important contributions, and indicate how it is intended to validate these errors by post-launch experiments. An idea of the range of experiments used in previous altimeter missions may be found in the TOPEX/Poseidon special issue on geophysical validation (*J. Geophys. Res.*, 99(C12)); a more detailed and complete description of the CryoSat errors and their validation can be found in the CryoSat calibration and validation concept document (Wingham et al., 2001).

6.1. The instrument system errors ε_{1b}

Notwithstanding the comments of the introduction to this section, a summary of the instrument system contribution $L_2^{(\text{h})}\varepsilon_{1\text{b}}$ to the elevation error budget is useful. In SARInM, differentiation of Eq. (20) provides

$$\delta z_{\text{ice}} = \delta z_{\text{sat}} + \hat{n}_z \delta r_{\text{poca}} + r_{\text{poca}}\delta\hat{n}_z \qquad (44)$$

so that the elevation error is generally that arising from the orbit, range and angle measurements. In SARM and LRM the angle error is not present. Table 3 shows the contributions

$$E\{(L_2^{(\text{h})}\varepsilon_{1\text{b}})^2\}$$

in the three modes. These are the 'single-shot' contributions associated with the ~20 Hz measurements. The orbit error is based on previous experience with the DORIS system (Section 2.2) with an allowance for the orbit altitude, and the range error is determined from Monte-Carlo simulation of the kind illustrated in Fig. 15. The source of these errors are familiar from pulse-limited altimetry. The angle error of the SARInM is not, and it is described in more detail in Appendix B.

Post-launch, the relative validation of the orbit and range error will be performed by comparison, over the ocean, with the ENVISAT RA2 and Jason sea-surface elevations. The separation of these two errors from each other, and from errors in the various corrections to the various measurements, depends on examining their spatial, temporal and spectral behaviour. The inclusion of a laser retroreflector in the payload (Section 2.2) also allows to an extent a validation of the orbit error separately from the range error. An absolute calibration of the angle error will be performed using a transponder located in Svalbard (which maximises the number of passes). Analysis of the transponder measurements also provides a verification of the along-track point target response (i.e., of the beam formation described in Section 3.1), and any datation correction to be applied to the payload source packets. A validation of the angle error will also be attempted by rolling the spacecraft over the ocean, although, pre-launch, it is not obvious that the ocean surface gradient is stable enough for this purpose.

It is also of interest to compare the performance of Table 3 with conventional ocean, pulse-limited altimetry, for which a 2 cm range precision of a 1 second average is typical. Were the SARM used for this purpose, the equivalent figure for the range precision is 2.6 cm, i.e., about the same level of performance. (This does not quite compare like-with-like. The SARM values refer to the empirical retracker illustrated in Fig. 15; a retracker designed specifically for the ocean surface (e.g., Jensen, 1999b) may improve on this performance.)

Table 3
Instrument system contributions to the elevation error

	SARInM	SARM	LRM
Orbit error (cm)		6	
Range error (cm)	14	10	7
Angle error (cm)	1.5		
RSS total	15	11.6	9.2

6.2. Errors in ice sheet trends

In measurements of $\hat{\hat{h}}$, the dominant sources of error are ε_{1b} and $\varepsilon_2^{(h)}$, but their relative importance is a strong function of spatial scale. Taking first ε_{1b}, $L_2^{(h)} = L_2^{(h)}$, and all of the entries to Table 3 make a contribution. Table 3 shows that, in SARInM and LRM, the range error at a point dominates the orbit and angle errors. However, the range error is (almost) complete de-correlated point-to-point. Its variance in a spatial average reduces as the number of cross-overs. This is not true of the angle or orbit errors. The angle error is better taken as reducing with the number of orbits (see Appendix 2 for further comment). The same is true of the orbit, but in averages of the largest areas and times, the orbit error is fundamentally limited by the accuracy with which its reference system is known, and this is unlikely in a three-year mission to be known better than 0.5 cm. The simplest description of the instrument system contribution to an averaged elevation rate is

$$
\begin{aligned}
&E\{(L_{hl}^{(\dot{h})} L_2^{(\dot{h})} \varepsilon_{1b})^2\} \\
&= \frac{1}{T_d^2}\left(2\frac{E\{\delta r_{poca}^2\}}{N_{over}} + 4\frac{E\{\delta z_{sat}^2\} + r_{poca}^2 E\{\delta \hat{n}_z^2\}}{N_{orbits}} + b_{orb}\right).
\end{aligned}
\tag{45}
$$

In Eq. (45), N_{over} and N_{orbits} are the total number of crossovers and orbits in $\mathfrak{I}_t$ and $\mathfrak{I}_{t_1}$ (see Eq. (35)), here assumed to equal each other. In detail, the coefficients in Eq. (45) depend on how, exactly, the cross-overs are formed and whether summation over t_1 (Section 5.1) is employed. Here, the factor 4 reflects the differencing operations of Eqs. (34) and (36), the factor 2 because, typically, four ranges are used in the calculation of Eq. (34). b_{orb} accounts for unknown drift in the orbit reference system.

Turning now to $\varepsilon_2^{(h)}$, it will be recalled that this error arises because the echo is scattered from a situation different from that assumed in Section 4.1. These differences arise generally because the geometry of the ice sheet is different from that assumed, the scattering behaviour is different, or because the atmospheric refraction models are in error.

Elevation errors from un-modelled ice sheet topography have two effects. Firstly, topography broadens the leading edge of the echo, and (much like waves on the ocean) increases the speckle contribution to δr_{poca}. The effect is considerable, and δr_{poca} may be two or three times larger than the value given in Table 3. It remains point-to-point independent, however, and may be accommodated in practice by estimating $E\{\delta r_{poca}^2\}$ from the data using single-cycle cross-overs, before applying the estimate of Eq. (45). The second effect of topography, relevant only to the LRM measurements, arises from off-nadir-ranging. It is partially corrected by a 'slope-in-

duced error' correction (Brenner et al., 1983). However, the subtraction Eq. (34) of $L_{hl}^{(\dot{h})}$ removes time-invariant errors from the measured elevation change, and the residual slope-induced error is of this kind.

Fluctuations arising from un-modelled scattering behaviour certainly occur, but the most obvious of these are removed by the correction described in Section 5.1. A residual scattering error in what remains is not easy to identify. In many areas of the Antarctic and Greenland ice sheets, time-series of elevation change that result once all known corrections are applied, are dominated by annual cycle. The amplitude of these cycles echoes the pattern of accumulation and is very approximately 30% of the water equivalent mean accumulation, with a minimum in the summer. It is entirely possible that these are the elevation expression of thermally-driven changes in the near-surface densification rate; it is equally possible that part of the signal results from changes in the near surface density causing variations, unrelated to the total energy, in the relation between the electromagnetic 'surface' and the physical surface.

Disentangling the two from the satellite measurements themselves is not possible because both may be expected to be functions of surface temperature, which in turn is strongly correlated with accumulation rate. As part of the validation, two sets of experiments are planned. First, the annual cycle of elevation at three separated sites in the southern Antarctic Peninsula will be investigated using a modification of the 'coffee-can' method of mass balance observation (Hamilton and Whillans, 2000). In this method, the motion of a 'can' buried in the firn is measured using GPS. By distributing several cans through the firn column, their relative motion, and hence the densification, can be observed. The addition of a sonic transducer tied to the GPS also determines the motion of the surface. Instrument packages including an automatic weather system (AWS) capable of continuous sampling throughout the year have been installed by British Antarctic Survey in austral summer 2004/5. Second, experiments are planned to investigate in detail the relationship between the near surface density and radar backscatter. Traverses of the EGIG line in Greenland, and of the Devon Ice Cap in Canada and the Austfonna ice cap in Svalbard will take place in Spring and Autumn 2004 and 2005, in which detailed, 2 cm resolution profiles in density will be measured using neutron probes (Morris and Cooper, 2003). These traverses will be overflown by an 13.5 GHz airborne radar ('ASIRAS') with 1 GHz bandwidth (12 cm resolution). The aircraft is also equipped with a GPS-tied laser altimeter, providing surface elevation changes and to range calibrate the radar.

We consider briefly errors in the atmospheric refraction corrections. At a point, these may amount in total to a few cm. However, because total electron content

is a minimum at the poles, and because the intensely cold ice sheet atmosphere is dry, the total value of these corrections when averaged on any scale is small (see Table 2), and the contribution to the error in any trend may be very small indeed. This is a distinct situation from that of observing sea-level rise, where atmospheric correction errors are important, because sea-level rise uncertainties are one to two orders of magnitude smaller than those connected with ice sheets.

A final aspect that forms part of the validation is to determine the performance over regions of complex ice cap and glacier geometries. The orbit and payload have been designed to observe the large, polar ice sheets. Nonetheless, SARInM data will be collected over all of the Earth's ice bodies (Section 2.5) in order that, at least experimentally, the performance of the SIRAL instrument over these ice bodies may be evaluated. As noted at the end of Section 3.2, when surface slopes exceed 0.8°, the echo loses its leading edge and the geometry becomes similar to that of a sideways-looking SAR interferometer. Specific experiments are planned in regions of glaciated Svalbard to compare 'swath-mode' retrievals of elevation from SIRAL echoes with that of airborne laser surveys. Should these prove successful, it is planned to develop, post-launch, verified algorithms for use in the operational environment.

6.3. Errors in sea-ice thickness

In contrast to the ice sheets, the process $L_2^{(t_{ice})}\varepsilon_{1b}$ contains the differencing operation Eq. (26) that removes long-scale instrument system errors, particularly the orbit error. At its simplest, one may take for the instrument system error

$$
E\left\{ (L_2^{(t_{ice})}\varepsilon_{1b})^2 \right\}
$$
$$
= \left(\frac{\rho_{ocean}}{\rho_{ocean} - \rho_{ice}}\right)^2 E\{\delta r_{poca}^2\}\left(\frac{1}{N_{ice}} + \frac{1}{N_{ocean}}\right). \qquad (46)
$$

An obvious feature of Eq. (46) is worth noting numerically: errors in freeboard are magnified in the thickness by a factor 9.6.

Turning to the error $\varepsilon_2^{(t_{ice})}$, one needs immediately to state that any discussion of these errors is, today, necessarily somewhat theoretical. This is because, to date, no independent measurements exist of sea-ice thickness of the *same ice* as that observed by a satellite altimeter. Verification of the satellite observations has been performed by comparing satellite measurements of $\hat{t}_{ice}$, typically over 1 month and 10^4 km², with the corresponding estimate from submarine upward-looking sonar (ULS) estimates of the same quantity (see Fig. 21). Differences between these two estimates contain all of the terms in Eq. (42) *and* the corresponding terms arising in the ULS measurements, and distinguishing the source of

errors is not easy. Further, in contrast to the ice sheet measurements, the number density of sea-ice measurements from the ERS altimeters is typically quite low (as a result of the poor instrument resolution). In consequence, the error of Eq. (46) can remain dominant even in averages over large areas. Thus, the un-modelled errors $\varepsilon_2^{(t_{ice})}$, which are readily apparent in the measured ice sheet elevation change itself once the instrument system errors have been sufficiently averaged down, have remained hidden in the ERS ice thickness measurements, if indeed they are even present to an important degree. For this reason, a second objective of the validation is to obtain measurements that will distinguish the magnitude and contributions of $\varepsilon_2^{(t_{ice})}$ and $\varepsilon_{hl}^{(t_{ice})}$.

This said, there are two sources of error that may be foreseen. The first arises with the assumption (Section 4.2 and illustrated in Fig. 17(a)) that the scattering from sea-ice arises from the snow-ice, and not the air-snow, interface. This must be substantially true. On the other hand, some energy must be scattered from the air–snow interface and an error must be anticipated. Secondly, errors in the ocean and ice densities, and the snow-loading, will affect the thickness through Eq. (41). Estimates of the variability of these quantities (Wadhams et al., 1992; Radionov et al., 1996) provides, with Eq. (40), a thickness error variability of 12 cm from these sources. The scales of these errors are not known. This, however, may underestimate the error. This is because ridged ice is often formed from rafted blocks of ice that form cavities containing sea-water below sea-level and air above. Thus, it is possible that the average column density differs from that of sea-ice, and that Eq. (41) should be replaced with an ice density that is a function of thickness.

As has been noted, these errors can only be investigated by comparing the satellite observations of ice freeboard with in situ observations of freeboard, density and thickness. Because all these quantities vary rapidly on metre scales, and because the ice is moving, obtaining measurements of the *same* ice requires some care. Experiments are planned north of Greenland in Spring and Autumn of 2005 and 2006 to make such measurements. Airborne laser and radar measurements of ice and snow freeboard, helicopter measurements of ice thickness using an 'E–M bird' (Hass and Eicken, 2001), and (rather more restricted) surface observations of density will be made of ice observed using CryoSat. Real-time measurements of the ice motion will be obtained via satellite from free-floating buoys equipped with GPS. These measurements will be used to provide headings for the aircraft and helicopter, which travel at different velocities from each other and from the satellite, to try to ensure the same ice is observed by all three platforms. (A trial of this method carried out in 2003 successfully removed the effects of ice motion from simultaneous aircraft and helicopter flights.)

We now turn to the errors arising from the sea-levels in Eq. (26). Since the effect of the filter Ω_{ocean} is to remove long-scale errors, one is left with the short-scale error (that is, the interpolation error that arises in estimating quantities at the point **y** in Eq. (26) from the ocean elevations observed at $\mathbf{y}_j$) associated with the modelled mean sea-level and tidal variation, and the variability of the dynamic topography. The best estimate of the mean sea-level is that from averaging and interpolating the oceans elevation obtained over the entire mission duration. Since this involves a very large number of spatially dense observations, we anticipate the error arising from this source will be small. The error arising from un-modelled tidal variation and the variability of the dynamic topography may be estimated by examining the average spectrum of ocean elevation variability along an orbit. A typical variability at 10^4 km^2 is 19.2 cm in thickness (Peacock and Laxon, 2004). Since all these errors are short scale, their variance in larger averages will reduce in proportion to the area.

For the same reasons as over the ice sheets, as well as the removal of long-scale errors by Ω_{ocean}, we expect the atmospheric refraction error to be small in comparison with the variability error.

We now turn to the error $\varepsilon_{hl}^{(t_{ice})}$. This arises because the probability of observing ice in any thickness interval is less than that of its occurrence. Comparisons of ERS thickness measurements with submarine ULS data (see, for example, Fig. 21) show clear evidence that below 1 m of thickness the observation probability drops below that of occurrence, and drops more-or-less to zero for thicknesses less than 70 cm. The source of this error is the instrument resolution, which makes it unable, with ERS, to discriminate ice from water when the floe size is less than a few kilometres. Since thin ice often forms in leads of small spatial extent, the observation probability of thin ice is much reduced. (The source of the difference in the thicker ice between the two plots in Fig. 21 is less clear: it may as equally arise from the ULS sampling as it does from that of the altimeter.)

The magnitude and scales of this error from the SIRAL measurements is not easy to estimate from previous experience, because the improvement in resolution will improve the observation probability of thinner ice, and because submarine data are too few to provide the scales of the error. Since it is an error of omission, related to ice floe area, its estimation requires knowledge of the joint probability density function of ice area and thickness, which does not seem to exist today. Therefore, we plan to augment the in situ sea-ice thickness measurements described above with satellite imagery, from which the joint density may be estimated, and from which the minimum flow area detectable by SIRAL may be determined. In this way, we expect to characterise $\varepsilon_{hl}^{(t_{ice})}$ in terms of known parameters such as the thickness distribution and ice concentration.

6.4. Summary error budget

The aim of the CryoSat mission is to measure fluctuations of the perennial Arctic sea-ice, and in the elevation Antarctic and Greenland ice sheets and the obvious question is how accurately this will be achieved. The question cannot be answered precisely today because, first, some parameters, while easily determined post-launch, are not well known today, particularly the ice sheet elevation variance at orbit cross-overs, the observation probability over sea-ice, and the long-term stability of the orbit. It is nonetheless useful to provide an idea of the performance and one such estimate is shown in Table 4.

In compiling Table 4, we have taken 70° as a typical latitude. In an area of 10^5 km^2 and over 1 month, some 9500 echoes will be observed. Assuming an ice concentration of 90%, and an ice observation probability of 0.7, there will be some 6000 ice observations and 950 ocean observations. Entering these numbers in Eq. (46) together with the range error from Table 4 provides an error variance of 3 cm. This is smaller than the estimate of the error arising from ocean variability, which, at 10^5 km^2, is 6 cm. We accordingly expect the ocean variability error to exceed that of the ice elevations themselves. Turning to the ice sheets, we assume that the first and last three months of a three-year data set are used to estimate the average elevation change. At 10^4 km^2, there will be some 50 cross-overs formed from some 10 orbits. Entering these numbers in Eq. (45), and taking the variance of the elevation difference at a cross-over as three times the value in Table 4 (see Section 6.2), the dominant error source (8.4 cm) is the ice elevation difference error. On the other hand, at 13.8×10^6 km^2 (the total area of the Greenland and Antarctic ice sheets) the dominant error is that from the orbit. Table 4 assumes a 1 cm fluctuation over the three-year mission.

These estimates do not take account of those errors that from Sections 6.2 and 6.3, we expect are present, but whose magnitude is not known today. The figures in Table 4 justify a closer understanding of these errors. The value for Arctic sea-ice corresponds to a freeboard variability of 0.72 cm, and it is not clear today that the snow–ice interface may be determined this accurately. Similarly, at large-scales, a residual error in the annual cycle may well exceed the 1 cm that has been allowed for orbit drift. The validation experiments, briefly described above, are an essential part of forming, post-launch, an accurate estimate of the total error.

Table 4
Expected CryoSat performance

	Arctic Sea ice thickness	Ice sheet elevation change	
	1 month, 10^5 km^2 at 70°	10^4 km^2 at 70°	13.8×10^6 km^2
Performance	6.8 cm	3.1 cm yr^{-1}	0.33 cm yr^{-1}

7. Concluding remarks

The CryoSat mission is designed to investigate the Earth's ice mass fluxes in a more complete way than has been possible previously by overcoming the limitations imposed by the design of previous altimeters and their platforms. In contrast to the US satellite ICESAT, CryoSat retains a microwave radar, SIRAL, which improves on pulse-limited altimeter design in two respects. Firstly, the pulse-repetition frequency is increased, to allow coherent processing of the echoes along-track. This improves the resolution in the along-track direction to ∼300 m. In addition, because the illumination geometry becomes essentially one-, rather than two-dimensional (the 'line' approximation of Section 3), the area illuminated per unit time falls off rapidly across track, effectively reducing the across-track resolution to ∼1 km. This improvement in resolution will greatly improve on the poor sampling density over ice sheet margins and sea-ice floes that characterises the earlier generation of altimeters. Secondly, SIRAL has a second receiver placed across-track, permitting the precise location by across-track interferometry of the echo in regions of complex topography. Nonetheless, because the across-track geometry remains pulse-limited, the requirement on angular accuracy remains relaxed in comparison with a beam-limited instrument, and it has proved possible with careful design and construction to achieve the requirement with the SIRAL instrument. Finally, the CryoSat platform will enter a 92° inclination orbit, providing coverage beyond the 81.5° latitudinal limit of previous altimeter missions.

SIRAL is the first Earth-orbiting instrument of its type. While the processing of its data is based on the heritage of earlier missions, much of its detail is new. The algorithms are based on physical models of the surface character that have proved a useful basis in the past, and their performance has been investigated through simulation. Nonetheless, previous experience also shows that it is very likely these algorithms may be improved in the light of the post-launch data, and the principal aim of the algorithms described in this paper is to provide a useful basis for the verification and validation of the mission products. It is with this in mind that a complete 're-spin' of the entire mission data, based on optimised algorithms, is foreseen some 2.5 years into the mission. The same heritage also underpins our understanding of the likely errors, but it is clear that here too specific, post-launch experiments are needed to firmly establish errors in the computed ice fluxes.

Nonetheless, the performances given in Table 4 provide some insight into the scientific effectiveness of the mission. Taking the sea-ice figure first, Laxon et al. (2003) have shown that at a basin scale (3×10^6 km²), Arctic sea-ice has an inter-annual variability of 25 cm, almost completely determined by the melt season length.

However, the variability at smaller scales, and the extent to which advection contributes to it, is largely unknown; poor sampling densities result in too large an error to determine this. Cryosat will resolve this variability at scales smaller than 10^5 km² (Table 4, left column) and, over the three-year mission duration, provide a clear picture of the covariance of the thickness. Armed with this, it will become possible to determine whether the reduction in sea-ice mass deduced from sparse submarine records results from a long-term (40 year) trend, or is merely the result of the ephemera of inter-annual fluctuation.

Turning to the ice sheets, 13.8×10^6 km² is the total area of glacier ice on Earth, and 1 cm of ice per year over this area is the equivalent of 0.35 mm yr⁻¹ of eustatic sea-level rise. This is of itself a smaller uncertainty than that today associated with the cryospheric contribution to sea-level change. Again, however, we have already learnt much of what is occurring in Antarctica and Greenland from previous satellite missions and (in Greenland) airborne campaigns. The greatest uncertainty today resides in the areas of Antarctica that have yet to be provided with dense altimeter coverage. Given that the performance at 10^4 km² (Table 4, middle column) is actually obtained over the Antarctic margins and Peninsula, it will be possible, with CryoSat, to reduce the uncertainty of the present cryospheric contribution to sea-level change ($\sim$0.1 mm yr⁻¹) to that associated with other sources of ocean volume.

Appendix A. The retracking function f_ψ

The retracking function is given by

$$f_\psi(t; a, \sigma, t_0, c, \alpha, n) = a \exp(-h^2(t/t_p)), \tag{A.1}$$

where t_p is the compressed pulse duration (3.125 ns), and

$$h(s) = \begin{cases} \frac{1}{10}(s - s_o) - 2.5 + \frac{n\sigma}{10} & s < s_o - n\sigma, \\ b_0 + b_1\left(s - s_o - \frac{\sigma}{2}\right) + b_2\left(s - s_o - \frac{\sigma}{2}\right)^2 \\ \quad + b_3\left(s - s_o - \frac{\sigma}{2}\right)^3 & s_o - n\sigma < s < s_o - \frac{\sigma}{10}, \\ \frac{1}{\sigma}\left(s - s_o - \frac{\sigma}{2}\right) & s_o - \frac{\sigma}{10} < s < s_o + \frac{\sigma}{2}, \\ \frac{1}{\sigma}\left(s - s_o - \frac{\sigma}{2}\right) + a_2\left(s - s_o - \frac{\sigma}{2}\right)^2 \\ \quad + a_2\left(s - s_o - \frac{\sigma}{2}\right)^3 & s_o + \frac{\sigma}{2} < s < s_o + 2\sigma, \\ -\log^{1/2}\left[\frac{ce^{-\alpha(s-s_o)}}{a(s-s_o)^{1/2}}\right] & s > s_o + 2\sigma. \end{cases}$$

(A.2)

The fitted parameters are those in the argument of in (A.1) and are subject to the constraints $a_{max}/100 < a < 10a_{max}$, where a_{max} is the maximum sample value in the echo, $2 < \sigma < 30$, $-0.1 < \alpha < 0.1$, $2 < n < 10$ and $0.01a_{max} < c < 99a_{max}$. The remaining parameters which appear in (A.2) are eliminated by requiring that h and its first derivative are continuous.

Appendix B. The SARInM angle error

In this appendix, we consider in more detail the interferometric contribution to the ice elevation error. This contribution is the final term of Eq. (44) describing the effect of an error in the direction vector $\hat{\mathbf{n}}_{poca}$ in calculating using Eq. (20) the vertical component z_{ice} of the point of closest approach. (There is a subtlety in Eq. (44) in that z_{ice} and $\hat{n}_z$ are the vertical components in the elliptical WGS co-ordinate system. However, one may show that for the purposes of calculating errors, one may take a local Cartesian frame to a good accuracy.) $\hat{\mathbf{n}}_{poca} + \delta\hat{\mathbf{n}}_{poca}$ is obtained as the solution of the simultaneous equations Eq. (21). Of these, the vector $\hat{\mathbf{n}}_2$ is very accurately known (see Section 2.2), and to the accuracy that concerns us, $\hat{\mathbf{n}}_{poca} + \delta\hat{\mathbf{n}}_{poca}$ is constrained by the second equation of Eq. (21) to fall within the across-track plane. In this case one may set $\hat{n}_z + \delta\hat{n}_z = \cos(\omega_{poca} + \varepsilon_\omega)$, where ω_{poca} is the angle $\hat{\mathbf{n}}_{poca}$ makes with the nadir direction.

The final term of Eq. (44) is then $-r_{poca}\sin(\omega_{poca})\varepsilon_\omega$ to first-order in the error ε_ω. This error, which is that associated with a beam-limited instrument, would places a heavy demand on the pointing knowledge of the interferometer baseline. However, for the smooth surfaces we assume, $\hat{\mathbf{n}}_{poca}$ is parallel to the surface normal at the POCA. If we take Eq. (20) to estimate the elevation of the nearby point on the surface in the direction given by the angle $\omega_{poca} + \varepsilon_\omega$, rather than by the angle ω_{poca}, the first order error is exactly cancelled by the first-order change in elevation between the POCA and the nearby point. Thus to lowest order, the final term of Eq. (44) may be taken to be $-r_{poca}\cos(\omega_{poca})\varepsilon_\omega^2/2$. This is second

order in ε_ω, and considerably relaxes the pointing knowledge requirement on the spacecraft.

The error ε_ω arises in the third equation of Eq. (21) through measurement errors in the baseline vector $\hat{\mathbf{m}}_b$ and $\sin\rho_{poca}$. In practise, the attitude control system holds $\hat{\mathbf{m}}_b$ close enough to $\hat{\mathbf{n}}_3$ that the contribution (to the error) of pitch and yaw may be ignored. One then has simply

$$\varepsilon_\omega^2 = (\varepsilon_\rho + \varepsilon_\eta)^2 \tag{B.1}$$

where ε_η is the error in the roll angle of the interferometric baseline, and ε_ρ is the measurement error in ρ_{poca} (see (4.6)).

Monte-Carlo simulation shows that the speckle contribution to ε_ρ has a standard deviation of 67 μrad, while the internal calibration accuracy (Section 2.1) is estimated to be 45 μrad. More important are the biases arising from the antennas' phase difference pattern (Fig. 3(b)), and from the difference between the functional form of $g(\tau, \chi_i)$ and the actual behaviour of the multi-looked phase (Fig. 11(b)). Both of these depend on $\sin\rho_{poca}$, which is not known a priori, and their correction would require an iterative step. To date an iterative step is not included in the *level 2* processing (Section 4.1), and these biases will contribute, typically, 100 μrad. The dominant contribution to ε_η is a bias expected to arise from uncorrected thermal deformation of the star tracker-bench-antenna assembly. A worst-case estimate of this bias is 131 μrad. A total worst-case assumption is then that the biases sum linearly, resulting in a total root-sum-square (RSS) error of 411 μrad, generating to a RSS elevation error of 6 cm. (When (B1) is dominated by bias terms, the variance of ε_ω^2 is approximately linear in the variance of $\varepsilon_\rho + \varepsilon_\eta$.) A more typical situation is perhaps that given when all the errors are root-sum-squared, in which case the RSS elevation error is 1.5 cm, which is the value given in Table 3. On the other hand, because the dominant contributions emerge from slowly varying functions, it is safer to assume the error decorrelates orbit-to-orbit, and not echo-to-echo.

References

Alexsandrov, Y.N., Bazilevskii, A.T., Kotel'nikov, V.A., Petrov, G.M., Rzhiga, O.N., Sidorenko, A.I. A planet discovered: results of Venus radar imaging from the Venera 15 and Venera 16 spacecraft. Sov. Sci. Rev. E. Astrophys. Space Phys. 6, 61–101, 1998.

Arthern, R.A., Wingham, D.J. The natural fluctuations of firn densification and their effect on the geodetic determination of ice sheet mass balance. Climatic Change 40, 605–624, 1998.

Arthern, R.A., Wingham, D.J., Ridout, A.L. Controls on ERS altimeter measurements over ice sheets: footprint scale topography, backscatter fluctuations, and the dependence of microwave penetration depth on satellite orientation. J. Geophys. Res. 106, 33471–33484, 2001.

Beaven, S.G. Laboratory measurements of radar backscatter from bare and sbow covered saline ice sheets. Int. J. Remote Sens 16, 851–876, 1995.

Brenner, A.C., Bindschadler, R.A., Thomas, R.H., Zwally, H.J. Slope-induced errors in radar altimetry over continental ice sheets. J. Geophys. Res. 88, 1617–1623, 1983.

Broecker, W. Unpleasant surprises in the greenhouse? Nature 328, 123, 1987.

Brown, G.S. The average impulse response of a rough surface and its implications. IEEE Antennas and Propagation AP-25, 67–74, 1977.

Benveniste, J. (Ed.) ENVISAT RA-2/MWR Product Handbook, European Space Agency Report PO-TN-ESR-RA-0050, Issue 1.2, 22 March 2002, European Space Agency, Noorwijk, The Netherlands, 2002.

Cartwright, D.E., Edden, A.C. Corrected tables of tidal harmonics. Geophys. J. R. Astron. Soc. 33, 253–264, 1973.

Curlander, J.C., McDonough, R.N. Synthetic Aperture Radar: Systems and Signal Processing. John Wiley & Sons, Inc., New York, 1991.

Francis, O., Mazzega, P. Global charts of ocean tide loading effects. J. Geophys. Res. 95, 11411–11424, 1990.

Francis, C.R. CryoSat Mission and Data Description, European Space Agency Report CS-RP-ESA-SY-0059, European Space Agency, Noordwijk, Netherlands, 78p, 2001.

Haardeng-Pedersen, G., Keller, K., Tscherning, C.C., Gundestrop, N. Modelling the signature of a transponder in altimeter return data and determination of the reflection surface of the ice cap near the GRIP camp, Greenland. J. Glaciol. 44, 625–633, 1998.

Hamilton, G.S., Whillans, I.M., Point measurements of mass balance of the Greenland ice sheet using precision vertical global positioning system, J. Geophys. Res. 105, 16259–16301, 2000.

Hass, C., Eicken, H. Interannual variability of summer sea-ice thickness in the Siberian and central Arctic under different atmospheric regimes. J. Geophys. Res. 106, 4449–4462, 2001.

Hayne, G.S. Radar altimeter mean waveforms from near-normal incidence ocean surface scattering. IEEE. Trans. Antenn. Propag. AP-28, 687–692, 1980.

IPCC. Changes in sea level, in: Houghton, J.T., Ding, Y., Giggs, D.J., Noguer, M., van der Linden, P.J., Dai, X., Maskell, K., Johnson, C.A. (Eds.), Climate Change: The Scientific Basis. Cambridge University Press, 881p, 2001 (Chapter 11).

Jacobs, S.S., Hellmer, H.H., M, C.S., Jenkins, A., Frohlich, R. Melting of ice shelves and the mass balance of Antarctica. J. Glaciol. 38, 375–387, 1992.

Jensen, J.R., Kilgus, C.C. The design of scanning, spaceborne radar altimeter for measuring polar iceProceedings of the International Geoscience Remote Sensing Symposium, IGARSS, vol. IV. IEEE, pp. 1641–1643, 1993.

Jensen, J.R. Angle measurement with a phase monopulse radar altimeter. IEEE Trans. Antenn. Propag. 47, 715–724, 1999.

Jensen, J.R. Radar altimeter gate tracking: theory and extension. IEEE Trans. Geosci. Remote Sens. 37, 651–658, 1999b.

Laxon, S., Peacock, N., Smith, D. High interannual variability of sea ice thickness in the Arctic region. Nature 425, 947–950, 2003.

Le Provost, C., Lyard, F., Molines, J.M., Genco, M.L., Rabilloud, F. A hydro dynamic ocean tide model improved by assimilating a satellite altimeter-derived data set. J. Geophys. Res. 103, 5513–5529, 1998.

Llewwllyn, S.K., Bent, R.B. Documentation and description of the Bent ionospheric model, AFCRL-TR-73-0657, Air Force Cambridge Research Laboratory, Hanscom Air Force Base, MA, 1973.

MacArthur. Design of the Seasat-A radar altimeter, in: Proceedings of the Oceans 1976: IEEE No 76CH1118-90EC, 10B-1-8, 1976.

McGoogan, J.T. Satellite altimetry applications. IEEE Trans. Microwave Theory Tech. MTT-233, 970–978, 1975.

Meier, M.F. Contribution of small glaciers to global sea level. Science 226, 1418–1421, 1984.

Morris, E.M., Cooper, J.D. Density measurements in ice boreholes using neutron scattering. J. Glaciol. 49, 599–604, 2003.

Nouel, F., Berthias, J.P., Deleuze, M., Guitart, A., Laudet, P., Piuzzi, A., Pradines, D., Valorge, C., Dejoie, C., Susini, M.F., Taburaiu, D. Precise Center-National-Detudes-Spatiales orbits for TOPEX/POSEIDON-is reaching 2-cm still a challenge. J. Geophys. Res. 99, 24405–24419, 1994.

Oppenheimer, M. Global warming and the stability of the West Antarctic ice sheet. Nature 393, 325–332, 1998.

Peacock, N.R., Laxon, S.W. Height determination in the Arctic Ocean from ERS altimetry. J. Geophys. Res. 109, doi:10.1029/2001JC001026, 2004.

Phallipou, L., Piau, P., Wingham, D.J., Mavrocordatos, C. High resolution radar altimeter for ocean and ice sheet monitoring, in: Proceedings of the IGARSS, Seattle, WA, July 1998, pp. 2020–2022, 1998.

Ponte, R.M. Sea level response to pressure forcing in a barotropic numerical model. J. Phys. Oceanogr. 21, 1043–1057, 1991.

Radionov, V.F., Bryazgin, N.N., Alexandrov, E.I. The snow cover of the Arctic Basin, APL-UW TR 9701, Applied Physics Laboratory, University of Washington, 95pp, 1996.

Rahmstorf, S., Marotzke, J., Willebrand, J. Stability of the thermohaline circulation, in: Krauss, W. (Ed.), The warm water sphere of the North Atlantic Ocean, Borntraeger, Stuttgart, pp. 129–158, 1996.

Raney, R.K. A delay/Doppler radar altimeter for ice sheet monitoring. in: Proceedings of the IEEE International Geoscience Remote Sensing Symposium IGARSS'95. IEEE, Florence, Italy, pp. 862–864, 1995.

Raney, R.K. The delay Doppler radar altimeter. IEEE Trans. Geosci. Remote Sens. 36, 1578–1588, 1998.

Ridley, J.K., Partington, K.C. A model of satellite altimeter return from ice sheets. Int. J. Remote Sens. 9, 463–474, 1988.

Rignot, E. Fast recession of a West Antarctic glacier. Science 281, 549–551, 1998.

Rothrock, D.A., Yu, Y., Maykutt, G.A. Thinning of the Arctic sea-ice cover. Geophys. Res. Lett. 26, 3469–3472, 1999.

Saastamoinen, J. Atmospheric correction for troposphere and stratosphere in radio ranging of satellitesGeophys. Monogr., vol. 15. American Geophysical Union, Washington, DC, 1972.

Shepherd, A.P., Wingham, D.J., Mansley, J.A.D., Corr, H.J. Inland thinning of Pine Island Glacier, West Antarctica. Science 291, 862–864, 2001.

Shepherd, A.P., Wingham, D.J., Mansley, J.A.D. Inland thinning of the Amundsen Sea sector, West Antarctica. Geohys. Res. Lett., 29, doi:10.1029/2001GL014183, 2002.

Tavernier, G., Granier, J.P., Jayles, C., Sengenes, P., Rozo, F. Integrated space geodetic systems and satellite dynamics. Adv. Space Res. 31, 1947–1952, 2003.

Wadhams, P., Tucker III, W.B., Krabill, W.B., Swiftt, R.N., Comiso, J.C., Davis, N.R. Relationship between sea ice freeboard and draft in the Arctic Basin, and implications for ice thickness monitoring. J. Geophys. Res. 97, 20325–20334, 1992.

Wahr, J. Deformation of the Earth induced by polar motion. J. Geophys. Res. 90, 9363–9368, 1985.

Wingham, D.J. A method for determining the average height of a large topographic ice sheet from observations of the echo received by a satellite altimeter. J. Glaciol. 41, 125–141, 1995.

Wingham D.J. (Ed.), CryoSat Science and Mission Requirements, Department of Space and Climate Physics, University College London, p. 56, 1999.

Wingham, D.J., Forsberg, R., Laxon, S.W., Lemke, P., Miller, H., Raney, K., Sandven, S., Scharroo, R., Vincent, P. CryoSat Calibration and Validation Concept Document, CPOM CS-PL UCL-SY-0004, CPOM, University College, London, 93p, 2001.

Wingham, D.J. Small fluctuations in the density and thickness of a dry firn column. J. Glaciol. 46, 399–412, 2000.

Wingham, D.J., Ridout, A.J., Scharroo, R., Arthern, R.J., Shum, C.K. Antarctic elevation change from 1992 to 1996. Science 282, 456–458, 1998.

Wingham, D.J., Phalippou, L, Mavrocordatos, C., Wallis, D. The mean echo and echo cross-product from a beam-forming, interferometric altimeter and their application to elevation measurement. IEEE Trans. Geosci. Remote Sens. 42, 2305–2323, 2004.

Wingham, D.J., Wallis, D.W. The rough surface impulse response of a pulse-limited altimeter with an elliptical antenna pattern, IEEE Trans. Antenn. Propag., submitted for publication.

Zwally, H.J., Brenner, A.C., Major, J.A., Bindschadler, R.A., Marsh, J.G. Growth of Greenland ice sheet: measurement. Science 246, 1587–1589, 1989.

Zwally, H.J., Schutz, B., Abdulati, W., Abshire, J., Bentley, C., Brenner, A., Bufton, J., Dezio, J., Handcock, D., Harding, D., Herring, T., Minster, B., Quinn, K., Palm, S., Spinhirne, J., Thomas, R. ICESAT's laser measurements of polar ice, atmsophere, ocean and land. J. Geodynam. 34, 405–445, 2002.